UNIVERSITY OF TWENTE.

Faculty of Electrical Engineering, Mathematics & Computer Science

MSc Thesis

Investigating the feasibility of PEMFCs for powering autonomous devices

Aiswarya Lakshmi Manikandan
MSc Systems & Control
Specialization: Biomechatronics

February 2024

Chair person:
Abelmann, Leon, prof.dr.ir.
External examiner:
Khalil, Islam, dr.
Supervisors:
Raman, Akash
Susarrey Arce, Arturo, dr.

University of Twente
P.O. Box 217
7500 AE Enschede
The Netherlands

MESA+ INSTITUTE

Preface

This research has been carried out under the Graduation Project (course code: 201100179) for the fulfilment of the program **MSc Systems & Control** with a specialization in **Biomechatronics** at the University of Twente, the Netherlands, P.O. Box 217, 7500 AE Enschede, The Netherlands, from 13-07-2023 until 05-02-2024.

Acknowledgements

I am deeply thankful for the successful completion of my Master's Graduation Project at the University of Twente, a collaborative effort that wouldn't have been possible without the invaluable contributions of many individuals.

I thank my family for constantly supporting me throughout this academic journey.

I would like to express my sincere appreciation to Prof. Islam S. M. Khalil, for his unique vision and for allowing me to be an integral part of this innovative project. His constant availability and insightful feedback were pivotal during the research. I thank my daily supervisor, Akash Raman, for his mentorship, constructive criticism and guidance throughout the project, and for providing me with the necessary resources. I extend my gratitude to Prof. Arturo Susarrey-Arce for sharing profound insights into Electrochemistry and allowing me to work in the chemical labs at the TNW department, University of Twente. I am grateful to Prof. Leon Abelmann, the chairman of my graduation committee, for conceptualising the idea of powering robots using fuel cells.

Special acknowledgement goes to Remco Sanders (Pino) for his prompt ideas and generous provision of resources that accelerated our research progress.

My deepest gratitude to my high school teachers for inspiring me to pursue academia and for their valuable lessons that have helped me in every stage of my academic journey.

Furthermore, I am indebted to the collaboration with my peers, Berfin Gürboğa, Justin R Harbers, Isabel Toebes, Astrid E Hornman, and Erwin van Renselaar, for their insightful discussions, and shared commitment to the project's progress.

I thank my friends for helping me during challenging times.

The learning journey has been truly remarkable, thanks to the collective efforts of everyone involved.

Abstract

Magnetically guided untethered devices are used in a variety of medical applications. These devices are typically powered by onboard battery units. Instead, hydrogen fuel cells are a promising alternative power source for such small-scale devices as they rely on a sustainable fuel, and do not require frequent charging or replacement. They function as electric power sources by utilising the electrochemical redox reaction of hydrogen and oxygen, using a solid-state proton exchange (polymer electrolyte) membrane (PEM).

A key first step towards the deployment of fuel cells in medical devices is to understand the effect of reducing the electrochemically active area of fuel cells to gain insights into the challenges of downscaling such devices. This thesis investigates the performance of PEM fuel cells (PEMFCs) when the active area is reduced, and when the fuel cell is supplied with reactants at different flow rates and with oxygen from air.

PEMFCs with three different active areas of electrodes, 3.5$\times$3.5, 2.7$\times$2.7, and 1.6$\times$1.6 [cm^2] were designed, fabricated, and electrochemically characterised using a potentiostat. A maximum fuel cell output power of 0.3, 0.09, and 0.03 [W] (maximum power density of 0.0245, 0.0123, and 0.0117 [W.cm^{-2}]) was observed respectively. Mathematical modelling of the PEMFC was done to simulate the fuel cell response and to get insights into the activation kinetics which is one of the electrochemical aspects of a fuel cell. In the context of small-scale magnetic actuation, the smallest PEMFC with an active area of 1.6$\times$1.6 cm^2 was tested with an inductor coil (rated 130 mA, 150 mH, 8 Ω). The resistive behavior of the coil was captured at a power of 0.0277 W (0.0108 W.cm^{-2}). The challenges and recommendations for using PEMFC as power sources are presented.

Keywords: PEMFC, active area, activation overpotential, Open Circuit Voltage (OCV), reactant flow rates, PEM electrolyzer, PEMFC modelling

Contents

List of Figures

List of Tables

Nomenclature

0.1 Abbreviations

CV	Cyclic Voltammetry
DC	Direct Current
FFP	flow field plate
MEA	membrane electrode assembly
PEEK	Polyetheretherketone
PEM	proton exchange membrane (or) polymer electrolyte membrane
PEMFC	PEM fuel cell
STP	Standard Temperature and Pressure (298.15 K, 1 bar)

0.2 Constants

F	Faraday's constant [96485 C.mol^{-1}]
R	gas constant [8.314 J.K^{-1}.mol^{-1}]

0.3 Quantities

I_0	fuel cell exchange current [mA]
I_{EL}	electrolyzer current [mA]
I_{FC}	fuel cell load current [mA]
I_{L}	fuel cell limiting current [mA]
E_0**, OCV**	Open circuit voltage (or) no load cell potential [V]

E_{FC}	fuel cell potential [V]
n	number of electrons transferred in the cell reaction [no units]
$\dot{n}$	Molar flow rate [mol.s^{-1}]
R_{FC}	Ohmic resistance of a PEMFC [Ω]
R_{L}	winding resistance of the inductor coil [Ω]
T	fuel cell operating temperature [295.12 K]
z	number of electrons per mole [no units]
α	(charge) transfer coefficient [no units]
η_{act}	activation overpotential [V]
η_{Ohm}	Ohmic overpotential [V]
η_{con}	concentration overpotential [V]

Chapter 1

Introduction

Untethered devices (UDs) have been used in medical applications such as surgical operations, precise drug delivery, and endoscopic procedures. These devices are actuated to manoeuvre through a bio-fluid to carry out various tasks. The actuation methods include ultrasound [1], [2], external magnetic fields [3], radio frequency signals [4], and light [5]–[7].

Magnetically actuated untethered devices (UMDs) use magnetic torque to move in the bio-fluid [8]. The magnetic torque is obtained as a cross product of magnetic dipole moment and magnetic field. The sources of dipole moment and magnetic field could be a permanent magnet or a current-carrying inductor coil. The magnetic dipole moment is usually generated inside the UMD and the magnetic field is applied externally (Fig. 1.1).

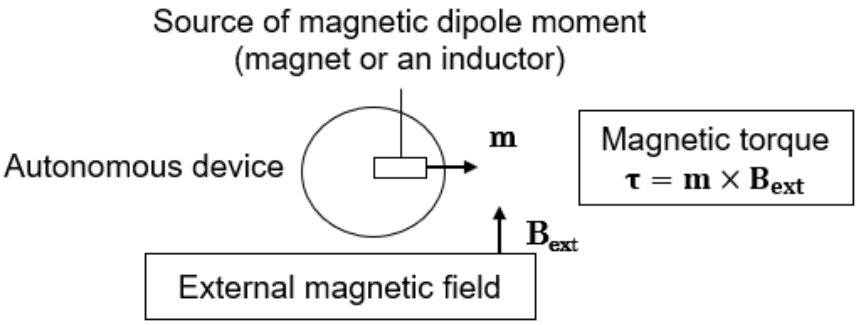

Figure 1.1: An illustration of magnetic torque to actuate (move) a device. The magnetic torque is a product of magnetic dipole moment produced inside the device and an external magnetic field.

There are two ways to obtain the magnetic torque. The most commonly adopted approach for actuating a UMD is to use an onboard stationary magnetic element,

such as a permanent magnet as the source of static dipole moment. An external dynamic magnetic field is provided by inductor coils or magnets attached to a moving robot [9], [10]. This external magnetic field is changed to manipulate the position and orientation of the UMD.

On the other hand, the second approach accomplishes magnetic actuation by generating a dynamic magnetic dipole moment inside the UMD. The dynamic magnetic dipole moment is created by passing a time-varying (dynamic) current through an inductor coil inside the UMD. The UMD's displacement and orientation are manipulated by altering the magnetic dipole moment produced by the onboard coil while the UMD is situated in a static external magnetic field [11]. The UMD requires an onboard circuit, like an oscillator to generate dynamic current to the coil. This approach eliminates the problem of interference between the external dynamic magnetic field source and other medical equipment in the vicinity, thereby reducing the complexity of external control. Furthermore, an onboard circuit provides room to integrate different sensors that could be used for diagnostics [7], which is not possible if the UMD only had a stationary magnetic element controlled by an external dynamic source as seen in the first approach.

Given that this approach has been less explored, this thesis work uses the second idea as a motivation to have an onboard circuit to drive a coil dynamically for a UMD.

When current I is passed through an inductor coil with n_{L} number of windings and radius r_{L}, the magnetic moment m generated by the coil is given as follows,

$$m = \pi n_{\mathrm{L}} I r_{\mathrm{L}}^2. \tag{1.1}$$

When the coil is placed with its axis perpendicular to an external magnetic field B_{ext}, a magnetic torque τ is generated,

$$\tau = m \times B_{\mathrm{ext}}. \tag{1.2}$$

A schematic representation is illustrated in Fig. 1.2.

PEM fuel cells as onboard power sources

Untethered devices (UDs) are often powered by onboard batteries that require recharging or replacement, which limits the operating time. This challenge can be addressed by using an energy harvester that either actuates the UD based on external sources like an external magnetic field [9] or derives energy from the environment like photovoltaic UDs [6].

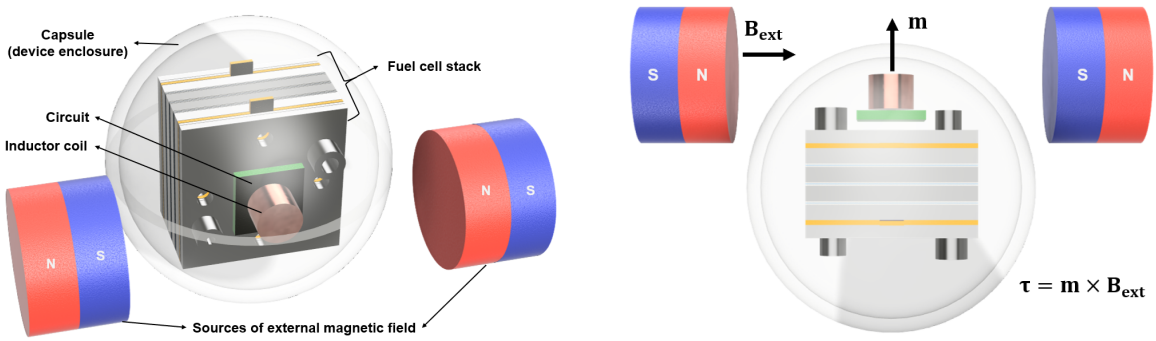

(a) (b)

Figure 1.2: (a) Schematic representation of using a fuel cell stack as an onboard power source for a magnetically actuated device (b) Top view of the idea of magnetic actuation for an UMD using fuel cell(s) as power source.

Fuel cells are electric power sources that can be used for a continuous supply of electric power, provided they have a continuous supply of chemical fuel. There are different kinds of fuel cells: PEM fuel cell (PEMFC), direct methanol fuel cell (DMFC), and solid oxide fuel cell (SOFC) to name a few. Most of them use hydrogen as fuel. Among them, PEMFCs have the following advantages over other kinds of fuel cells [12], [13]:

- PEMFCs require hydrogen and oxygen to generate electric power and water as a byproduct. DMFCs require methanol as fuel, and SOFCs require carbon monoxide. The fuels for the latter two cell types contribute to greenhouse gas emissions.
- PEMFCs can operate in ambient temperature and pressure.
- They are portable, faster to start operating, and suitable for small-scale applications.

Wang *et al.* [14] presented the effects of different operating parameters on the fuel cell performance, such as operating pressure, temperature, humidity, and humidification temperatures of reactants. Operating fuel cells at high temperatures (maximum 80 °C) and high pressures (3.7 bar) has been shown to increase fuel cell performance. The work also shows that an increase in humidification temperature increases the fuel cell performance. Humidification of reactants is shown to decrease the fuel cell performance especially when high load currents are drawn due to the limited concentration and faster consumption of reactants [15].

Artal *et al.* [16] used ultracapacitors to store power supplied by a fuel cell and used it to drive a mobile robot. The use of fuel cell stacks for mobile robots has

been carried out by researchers [17], [18]. These studies show that an intermediate power storage unit between the fuel cell and the load ensures continuous operation and that matching the power from the supply unit (fuel cell) and load (actuators in the robot) is a crucial step to ensure that the load can be driven using fuel cells.

However, the literature on the use of fuel cells for powering robotic devices is not very extensive because most of the robot applications take place in a shorter time duration which can be done using batteries. There are also the challenges of using fuel cells as onboard power sources such as onboard fuel storage and encapsulating a fuel cell stack and associated tubing inside the robot body.

Thangavelautham *et al.* [19] used a lithium hydride reactor to supply hydrogen to a PEMFC stack in a controlled manner for powering a mobile robot (Fig. 1.3). Van Renselaar *et al.* [20] modelled the relations between the size (radius) of a capsule-shaped UMD to the current drawn by its onboard electromagnetic coils and the velocity of the UMD in a liquid, correlating its electrical and mechanical characteristics of a capsule-shaped UMD.

Kesner *et al.* [21] proposed a similar idea of using miniaturised hydrogen fuel cells for a spherical untethered device with onboard electronics in the context of space robots for extraterrestrial exploration. They analysed the feasibility of the proposed 'Microbot' moving in an extraterrestrial environment and provided recommendations for each sub-system in the 'Microbot' such as fuel cells, fuel storage, electronics and actuator. The use of fuel cells for small-scale (in the range of a few centimetres) robot applications is ongoing.

Nonetheless, providing a stable source of hydrogen for PEM fuel cells is a challenge. Using hydrogen-producing bacteria is an alternative source of hydrogen for fuel cells. Bacteria are commonly present in liquid-phase biological environments [22]–[24], such as the bloodstream in an animal artery [25]. Microbial fuel cells (MFCs) are electrochemical energy harvesters that utilise hydrogen produced by microbial action to generate electric power. Harnessing electric power from a biochemical environment for autonomous robots is a novel approach for energy transduction and is a motivation for this project [17], [26].

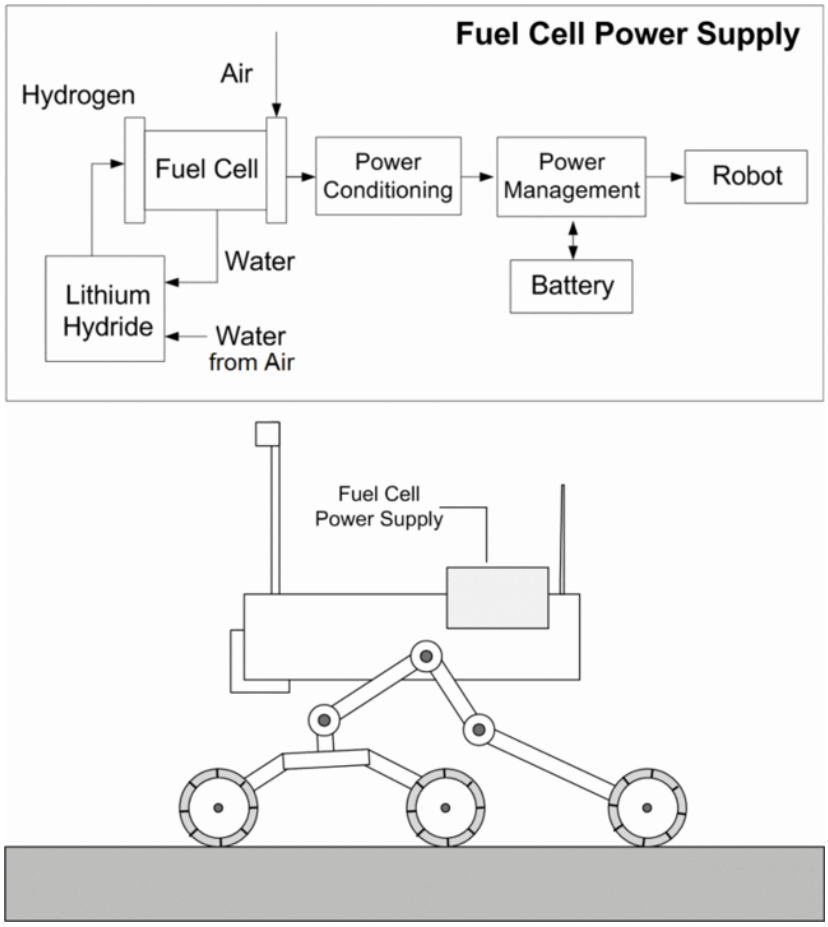

Figure 1.3: A robot powered by a PEMFC stack using a lithium hydride reactor as a fuel source for the PEMFC stack [19].

1.1 Objectives

The goal of this work is to investigate the feasibility of PEM fuel cells as an onboard power source for magnetically actuated devices. To understand how fuel cells perform upon miniaturisation, PEMFCs with three different active areas of electrode, 3.5×3.5, 2.7×2.7, and 1.6×1.6 [cm^2] were designed, fabricated, and electrochemically characterised using a potentiostat. A PEM electrolyzer was used to supply reactants (hydrogen and oxygen) to the PEMFC at different flow rates. The effects of reactant flow rate, oxygen source, and active area on PEMFC performance were studied. Further, mathematical models of the PEMFC were compared with the experimental data.

1.2 Research questions

This project aims to answer the following questions:

1. Can a single-cell PEMFC be used as an onboard power source for an autonomous device?
2. In the context of downscaling onboard power sources for an autonomous device, how does the reduction in the active area of the PEM fuel cells affect the fuel cell performance?
3. What are the challenges involved in operating PEM fuel cells?

1.3 Outline of the report

Chapter 2 explains the operating principle and governing equations of a PEM fuel cell.

Chapter 3 explains the design of PEMFC components, assembly of a PEMFC, and integration with a fuel source (an electrolyzer).

Chapter 4 explains the experimental protocols conducted.

Chapter 5 analyses the results from the experiments.

The report is concluded in Chapter 6 with recommendations in Chapter 7.

Chapter 2

PEMFC Operating principle

A fuel cell utilises the reduction-oxidation (redox) reaction of its reactants to generate electric current (discharge of electrons) that is used to drive an electric load. In the case of a hydrogen fuel cell, the reactants are hydrogen (fuel) and oxygen, the product is water, and a solid-state proton exchange membrane (or) polymer electrolyte membrane (PEM)[1] is used. The redox reactions in a hydrogen PEMFC are given by the following equations,

$$\text{Anode (Oxidation):} \qquad 2\,H_2 \longrightarrow 4\,H^+ + 4\,e^- \tag{2.1}$$

$$\text{Cathode (Reduction):} \qquad O_2 + 4\,H^+ + 4\,e^- \longrightarrow 2\,H_2O. \tag{2.2}$$

The overall fuel cell reaction is given by

$$2\,H_2 + O_2 \longrightarrow 2\,H_2O. \tag{2.3}$$

Open circuit voltage (or) no load cell potential [V] (E_0, OCV)[2] is the potential difference between the electrodes when the fuel cell is not electrically loaded, i.e., when no current is drawn from the fuel cell. It is a function of the operating temperature, and partial pressures of the reactants and the product, such that

$$E_0 = E_\mathrm{r} + \frac{RT}{nF} \log\left(\frac{p^2_{\mathrm{H_2}} \cdot p_{\mathrm{O_2}}}{p^2_{\mathrm{H_2O}}}\right), \tag{2.4}$$

where, $n = 4$ is the number of electrons transferred in the cell reaction [no units] (n), and E_r is the standard cell potential at Standard Temperature and Pressure (298.15 K, 1 bar) (STP) [27], being 1.229 V [28], [29]. R and F are gas constant

[1] PEM also denotes polymer electrolyte membrane. In this text, both the notations are suitable.

[2] OCV and Nernst cell potential are different notations to represent no-load cell potential. In some texts, they are denoted as E_N.

[8.314 J.K^{-1}.mol^{-1}] (R) and Faraday's constant [96485 C.mol^{-1}] (F) respectively. T is the fuel cell operating temperature [295.12 K] (T).

The performance of a fuel cell is characterised by the fuel cell load current [mA] (I_{FC}) and the fuel cell potential [V] (E_{FC}), i.e., the I-E characteristics[3]. When the fuel cell is electrically loaded, i.e. connected to an external electrical load, current flows through the external circuit, and the cell potential subsequently decreases due to irreversible losses called overpotentials. There are three kinds of overpotentials in a fuel cell: activation overpotential [V] (η_{act}), Ohmic overpotential [V] (η_{Ohm}), and concentration overpotential [V] (η_{con}) (equation 2.5),

$$E_{\mathrm{FC}} = E_0 - \eta_{\mathrm{act}} - \eta_{\mathrm{Ohm}} - \eta_{\mathrm{con}}. \tag{2.5}$$

Fig. 2.1 shows a typical I-E or polarization characteristics of a fuel cell. The figure shows the relation between fuel cell load current and cell potential, and the different I-E regions where different overpotentials are dominant.

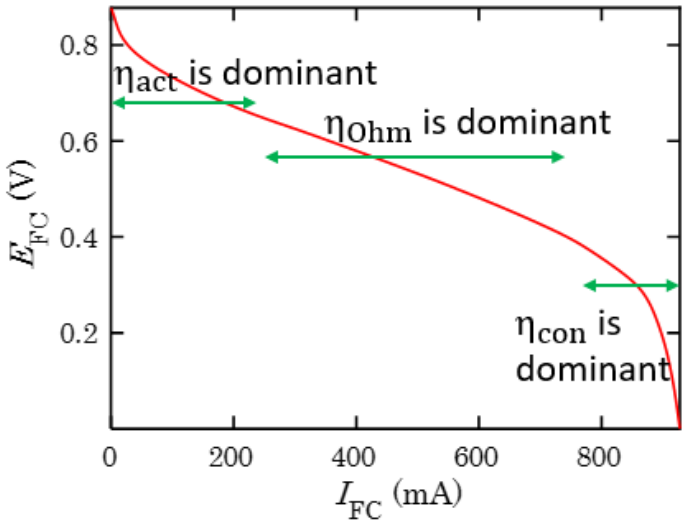

Figure 2.1: A typical I-E or polarization characteristics of a fuel cell.

2.1 Activation overpotential

The activation overpotential represents the minimum potential required to overcome the energy barrier for the redox reaction to occur, and it is dominant in the low-load current region [30]. Two parameters characterise the activation overpotential: (charge) transfer coefficient [no units] (α) and fuel cell exchange current [mA] (I_0).

[3] In this text, the cell potential is referred to as E [V]. Some texts use V to denote cell potential.

The transfer coefficient represents the contribution from the cathode and anode activation kinetics to cell potential losses when the fuel cell is loaded. The exchange current represents the reaction rate at equilibrium. The activation loss depends on the active area and material properties (such as porosity and structure) of the membrane and catalyst loading [31], [32]. Activation losses decrease with increasing transfer coefficient and increasing exchange current. Multiple sources provide two expressions for activation overpotential that are derived from the Butler-Volmer equation [33].

The Butler-Volmer equation (2.6) describes the activation kinetics for a fuel cell, relating the load current (I) to the rate of reaction represented by the exchange current (I_0),

$$I = I_0 \cdot \left(\exp\left(\frac{-\alpha_{\mathrm{C}} F(E - E_0)}{RT}\right) - \exp\left(\frac{\alpha_{\mathrm{A}} F(E - E_0)}{RT}\right)\right). \tag{2.6}$$

where α_A and α_C are the anodic and cathodic charge transfer coefficients respectively. E is the cell potential[4] and E_0 is the open circuit voltage. The activation overpotential is derived from the Butler-Volmer equation based on certain assumptions.

2.1.1 Assumption 1: Considering equal activation overpotentials at anode and cathode

When equal activation overpotentials are assumed at the anode and cathode, their transfer coefficients are approximately the same, say α,

$$\alpha_{\mathrm{A}} \approx \alpha_{\mathrm{C}} \approx \alpha. \tag{2.7}$$

Then, the derivation of activation overpotential from the Butler-Volmer equation is as follows:

$$I = I_0 \cdot \left(\exp\left(\frac{-\alpha F(E - E_0)}{RT}\right) - \exp\left(\frac{\alpha F(E - E_0)}{RT}\right)\right), \tag{2.8}$$

$$I = I_0 \left(-2\sinh\left(\frac{\alpha F(E - E_0)}{RT}\right)\right), \tag{2.9}$$

$$\Rightarrow \frac{\alpha F(E - E_0)}{RT} = -\mathrm{arcsinh}\left(\frac{I}{2I_0}\right), \tag{2.10}$$

$$\Rightarrow E - E_0 = -\frac{RT}{\alpha F} \cdot \mathrm{arcsinh}\left(\frac{I}{2I_0}\right). \tag{2.11}$$

[4] For the sake of simplicity, I and E are used to denote load current and cell potential only in this Section 2.1, since the Butler-Volmer relation is used to represent the electrochemical kinetics for fuel cells as well as electrolyzers.

For small load currents, the activation overpotential is dominant. The Ohmic and concentration overpotentials can be neglected. Hence the cell potential can be approximated as,

$$E \approx E_0 - \eta_{\text{act}}, \tag{2.12}$$

$$\Rightarrow -\eta_{\text{act}} = E - E_0, \tag{2.13}$$

$$-\eta_{\text{act}} = -\frac{RT}{\alpha F} \cdot \operatorname{arcsinh}\left(\frac{I}{2I_0}\right). \tag{2.14}$$

Thus, the expression for activation overpotential is given by equation 2.15,

$$\eta_{\text{act}} = \frac{RT}{\alpha F} \cdot \operatorname{arcsinh}\left(\frac{I}{2I_0}\right). \tag{2.15}$$

Some works computed activation overpotential using this expression [18], [20], [34].

2.1.2 Assumption 2: Neglecting anodic activation overpotential

The activation overpotential for Oxygen Reduction Reaction (ORR) is much greater than the activation overpotential for Hydrogen Oxidation Reaction (HOR) [32], [35]. Hence the anodic activation overpotential is often ignored [32],

$$\eta_{\text{act,C}} \gg \eta_{\text{act,A}} \quad \text{and} \quad \alpha \approx \alpha_{\text{C}}. \tag{2.16}$$

Under this assumption, the Butler-Volmer equation (2.6) is modified as follows,

$$I = I_0 \cdot \exp\left(\frac{-\alpha F(E - E_0)}{RT}\right), \tag{2.17}$$

$$\Rightarrow E - E_0 = -\frac{RT}{\alpha F} \log\left(\frac{I}{I_0}\right).$$

Ignoring the Ohmic and concentration overpotentials at low-load conditions,

$$E \approx E_0 - \eta_{act}, \tag{2.18}$$

$$\Rightarrow -\eta_{act} = E - E_0, \tag{2.19}$$

$$\eta_{\text{act}} = \frac{RT}{\alpha F} \cdot \log\left(\frac{I}{I_0}\right). \tag{2.20}$$

In this study, the anodic activation overpotential is not neglected. So, equation 2.15 is used as the expression to compute the activation overpotential in the mathematical model (Section 5.7).

2.2 Ohmic overpotential

The Ohmic resistance of a PEMFC [Ω] (R_{FC}) arises from the resistance to proton transport through the membrane and electron transport through the external load circuit [12], [32],

$$\eta_{\mathrm{Ohm}} = I_{\mathrm{FC}}(R_{\mathrm{ionic}} + R_{\mathrm{electronic}}), \tag{2.21}$$

$$\eta_{\mathrm{Ohm}} = I_{\mathrm{FC}} \cdot R_{\mathrm{FC}}. \tag{2.22}$$

The ionic resistance for proton transport depends on the surface area, thickness, and resistivity of the membrane. The electronic resistance depends on the electric path in the load circuit and electric contacts. The resulting Ohmic overpotential is dominant in the intermediate region of I-E characteristics, where the relation between the load current and cell potential is negatively linear.

2.3 Concentration overpotential

The concentration overpotential (also called mass-transport overpotential) represents the deviation of the concentration of reactants and products at the electrode-electrolyte interface from their concentrations in bulk. It is pronounced when the fuel cell is operated at high load currents, during which the reactants at the electrode surface are depleted, i.e., their concentrations reach zero quickly. In this study, the mass transport of reactants is considered by means of diffusion rather than convection [12]. The expression for the concentration overpotential is given by

$$\eta_{\mathrm{con}} = \frac{RT}{nF} \log\left(\frac{I_{\mathrm{L}}}{I_{\mathrm{L}} - I_{\mathrm{FC}}}\right), \tag{2.23}$$

$n = 4$ is again the number of electrons transferred in a redox reaction. I_L is the fuel cell limiting current [mA] (I_{L}). It is the load current when the concentration of reactants at the active sites of the catalyst are reduced to zero [28]. A fuel cell cannot be operated at load currents greater than its limiting current.

When the fuel cell is loaded, the expression for cell potential (equation 2.5) can be rewritten as 2.24,

$$E_{\mathrm{FC}} = E_0 - \frac{RT}{\alpha F}\mathrm{arcsinh}\left(\frac{I_{\mathrm{FC}}}{2I_0}\right) - I_{\mathrm{FC}} \cdot R_{\mathrm{FC}} - \frac{RT}{4F}\log\left(\frac{I_{\mathrm{L}}}{I_{\mathrm{L}} - I_{\mathrm{FC}}}\right). \tag{2.24}$$

2.4 Fuel cell efficiency

From the overall reaction for a hydrogen fuel cell (2.3), with the combination of hydrogen and oxygen, water is produced along with heat which accounts for thermal loss [12], [36]. The change in enthalpy of formation (ΔH) represents the heat released by the combustion of a fuel. The change in Gibbs free energy (ΔG) represents the electric energy produced,

$$E_r = \frac{\Delta G}{nF}. \tag{2.25}$$

The change in Gibbs free energy depends on the operating temperature (T) and the change in entropy (ΔS),

$$\Delta G = \Delta H - T \cdot \Delta S. \tag{2.26}$$

The maximum efficiency of a fuel cell is found as the ratio of change in Gibbs free energy to the change in enthalpy of formation,

$$\text{Efficiency, } \eta_e = \frac{\Delta G}{\Delta H} \cdot 100[\%] = \frac{E_{FC}}{1.481} \cdot 100[\%]. \tag{2.27}$$

The constants ΔH and ΔS depend on the thermodynamic data for hydrogen and the phase in which water is discharged.

Chapter 3

Experimental setup

The electrochemical system under study is a PEM fuel cell (PEMFC). PEMFCs of three different active areas were designed, fabricated, and assembled. A PEM electrolyzer is used as the reactants supply unit for the PEMFC. The design and functions of PEMFC components, and the integration of its reactants supply unit are explained below.

3.1 Components of a PEMFC

A PEMFC comprises the following components: end plates, gaskets, current collectors, flow field plate (FFP), and the membrane electrode assembly (MEA). MEAs of the aforementioned active areas with square lengths 3.5, 2.7 and 1.6 [cm] were procured (source: Bio-Connect). PEMFC components for each size were designed (using Fusion 360 and SOLIDWORKS 2022) and fabricated (Fig. 3.1). The thickness of each plate was chosen based on the available material thickness that was close to the range specified in literature [37]. The plates were fabricated using a Computer Numerical Control (CNC) machine and the gaskets were cut using a cutting plotter (CricutMaker 3). The components other than MEA were fabricated with four M3 holes at four corners for fastening. The components also featured two holes of diameter 2 mm for anode and cathode inlets (for hydrogen and oxygen), and for outlets to expel excess water. These holes facilitated the passage of reactants from the PEMFC inlets to the active area of MEA. The components of a PEMFC are shown in Fig. 3.1 and their functions are outlined in Table 3.1 with unique labels.

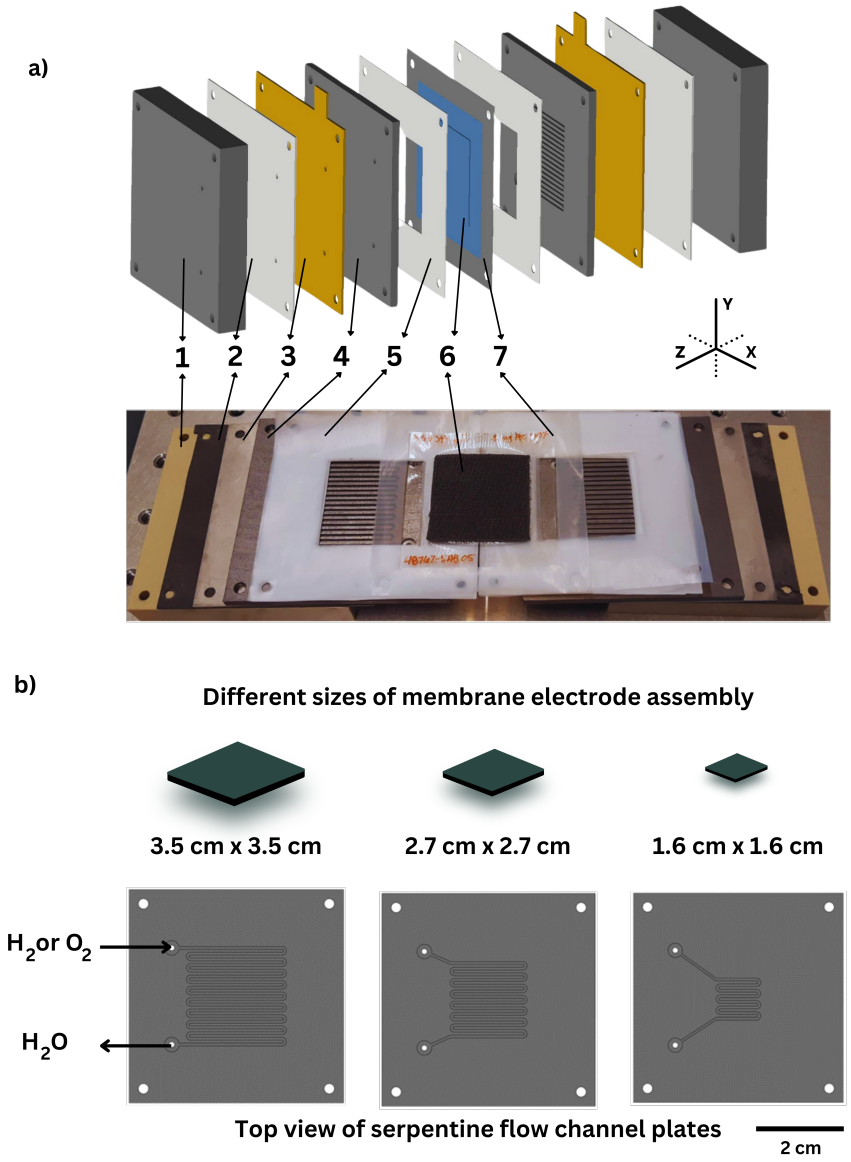

Figure 3.1: (a) Components of a single cell PEMFC; 1: end plate, 2: Viton gasket, 3: current collector, 4: flow field plate (FFP), 5: Teflon gaskets, 6: membrane electrode assembly (MEA), and 7: Teflon frame, (b) Membrane electrode assembly (MEA) and flow field plates (FFPs) of different active areas (square length of MEA: 3.5, 2.7, and 1.6 [cm]).

Table 3.1: Components of a PEMFC

Label	Component		Material	Purpose
1	End plate		PEEK	uniform compression across PEMFC stack
2	Gasket		Viton	leakage prevention, sealing
3	Current collector		Stainless steel (SS316L)	current collection
4	FFP		Graphite (G-10)	uniform distribution of reactants
5, 7	Gasket, frame		Teflon	leakage prevention, sealing
6	MEA	GDL	Carbon cloth (W1S1011)	diffusion of gaseous reactants
		Catalyst	0.5 mg.cm^{-2}, PtC (60%)	oxidation of hydrogen, reduction of oxygen
		PEM	D50-U	proton transport

The end plates provide uniform compression across the PEMFC. They were fabricated in Polyetheretherketone (PEEK) because of its higher permeation resistance to hydrogen [38], [39]. The holes of diameter 2 mm were milled with threads (thread port configuration: 1/4-28" flat-bottom) that enabled connecting suitable connectors to the Teflon tubing (inner diameter: 1.6 mm, outer diameter: 3.2 mm).

Stainless steel (SS316L) current collectors were chosen for current collectors due to its extensive availability, corrosion resistance, and cost-effectiveness.

Flow field plates (FFPs) regulate uniform distribution of reactants over the active area of PEMFC's electrodes[1]. They are also referred to as "bipolar plates" in literature when multiple fuel cells are used in a PEMFC stack. Graphite (grade G-10) was preferred over metal and composites for FFPs because of graphite's superior qualities in terms of corrosion resistance, electric conductivity, and chemical stability [40], [41]. Metal flow field (bipolar) plates require an anti-corrosion coating that increases the Ohmic resistance and manufacturing costs [42].

Single serpentine flow field geometry (Fig. 3.1(b)) was chosen for the FFPs owing to the geometry's advantages of uniform pressure distribution, better water management and effective distribution of reactants across the active area of electrode [43]–[45]. The FFPs were designed to ensure counter-flow of reactants in the anode and cathode channels, which has been claimed to yield higher cell efficiency [43], [46]. The flow field channels are designed with dimensions close to those mentioned in the literature [37], [41]: 1 mm depth, 1 mm rib width, and 1 mm width between channels. The holes of diameter 2 mm also featured counter-bore holes of diameter 5 mm to accommodate excess fluid and to avoid pressure drop across the channels. The design of end plates, current collectors and FFPs can be found in Appendix A.

The MEA is a combination of anode and cathode gas diffusion layers (GDL), anode and cathode catalyst layers, and a proton exchange membrane (PEM). The GDL facilitates the diffusion of gaseous reactants, water removal, electrical conduction between the current collectors and the catalyst layer, and heat dissipation. The catalyst layer enables the oxidation of hydrogen (fuel) and reduction of oxygen. PEM allows the transport of protons (H^+ ions), thereby completing the electrochemical circuit internally.

Gaskets were designed to ensure sealing and minimise leakage between the end plates and current collectors, and between FFPs and MEA. A Teflon frame was designed to hold the MEA in place. The sealing layers' thickness and quantity were chosen such that their compression does not exceed 12% (Appendix B.1). To minimize manufacturing costs for three sets of PEMFCs, one common pair of end plates

[1] Electrode refers to the catalyst and GDL [12].

and current collectors were fabricated. The other components were designed for each active area. Notably, all the components have the same square length (7.5 cm).

The plates were assembled using four stainless steel M3 nuts and bolts wrapped with Polytetrafluoroethylene (PTFE) Thread Seal Tape (Teflon T-27730A) to prevent short-circuiting across metal current collectors, at the four corners. Higher clamping torque results in lesser contact resistance. However, excess clamping compression could reduce the porosity of the MEA and damage the PEMFC plates [47]–[50]. Therefore, the nuts were fastened with a torque of 0.3 N.mm using a torque-limiting screwdriver. The effect of clamping torque on PEMFC performance is elaborated in Section 5.2.

3.2 Fuel Source Integration

A PEM electrolyzer (Horizon PEM Blue Electrolyzers, FCSU-010 model) was used to continuously supply hydrogen and oxygen to the PEMFC. The electrolyzer operates on the reverse reaction of a fuel cell. Hydrogen and oxygen are generated by the disassociation of water with the aid of external electrolyzer current [mA] (I_{EL}) supplied by a Direct Current (DC) source measurement unit (EA-PSI 6150-01 150 V/1.2 A). The redox reactions for an electrolyzer are as follows,

$$\text{Anode (Oxidation):} \quad 2\,H_2O \longrightarrow 4\,H^+ + O_2 + 4\,e^- \tag{3.1}$$

$$\text{Cathode (Reduction):} \quad 4\,H^+ + 4\,e^- \longrightarrow 2\,H_2 \tag{3.2}$$

The overall reaction in the electrolyzer is given by

$$2\,H_2O \longrightarrow 2\,H_2 + O_2 \tag{3.3}$$

The electrolyzer current (I_{EL}) was changed to control the Molar flow rate [mol.s^{-1}] ($\dot{n}$) of reactants to the PEMFC using Faraday's law of electrolysis,

$$\dot{n} = \frac{I_{\mathrm{EL}}}{zF}. \tag{3.4}$$

From the redox reaction for electrolysis of water (3.3), hydrogen is produced twice as much as oxygen. Hence, the number of electrons per mole [no units] (z) is 2 for hydrogen and 4 for oxygen. Similar to a PEMFC, the electrolyzer has two ports on each electrode side. The anode membrane is isolated from the cathode membrane.

On each side, one port is closed to prevent loss of generated gases. The anode and cathode of the other port were connected to the cathode and anode of PEMFC respectively. Teflon tubes were used for fluid connection between the electrolyzer and the PEMFC. The fluid connectors used in the setup are listed in Appendix B.2.

A potentiostat (BioLogic SP-150e and EC-Lab® software) was used to characterise the PEMFCs. There are 3 terminals in a potentiostat: working electrode, counter electrode, and the reference electrode (Appendix B.3). The potentiostat's working electrode was connected to the cathode current collector terminal of the PEMFC, and the potentiostat's counter electrode was connected to the anode current collector terminal of the PEMFC. Though the potentiostat is a 3-terminal device that can measure half-cell potentials, in this case, the reference electrode was shorted to the counter electrode and the potentiostat measured the overall potential drop across the fuel cell. It functioned as an electric load that draws load current from the PEMFC while measuring the cell potential, or applying a potential across the PEMFC's electrodes and recording the load current.

There was no control over the temperature, pressure and humidity of the fuel cell reactants. The experimental setup is shown in Fig. 3.2.

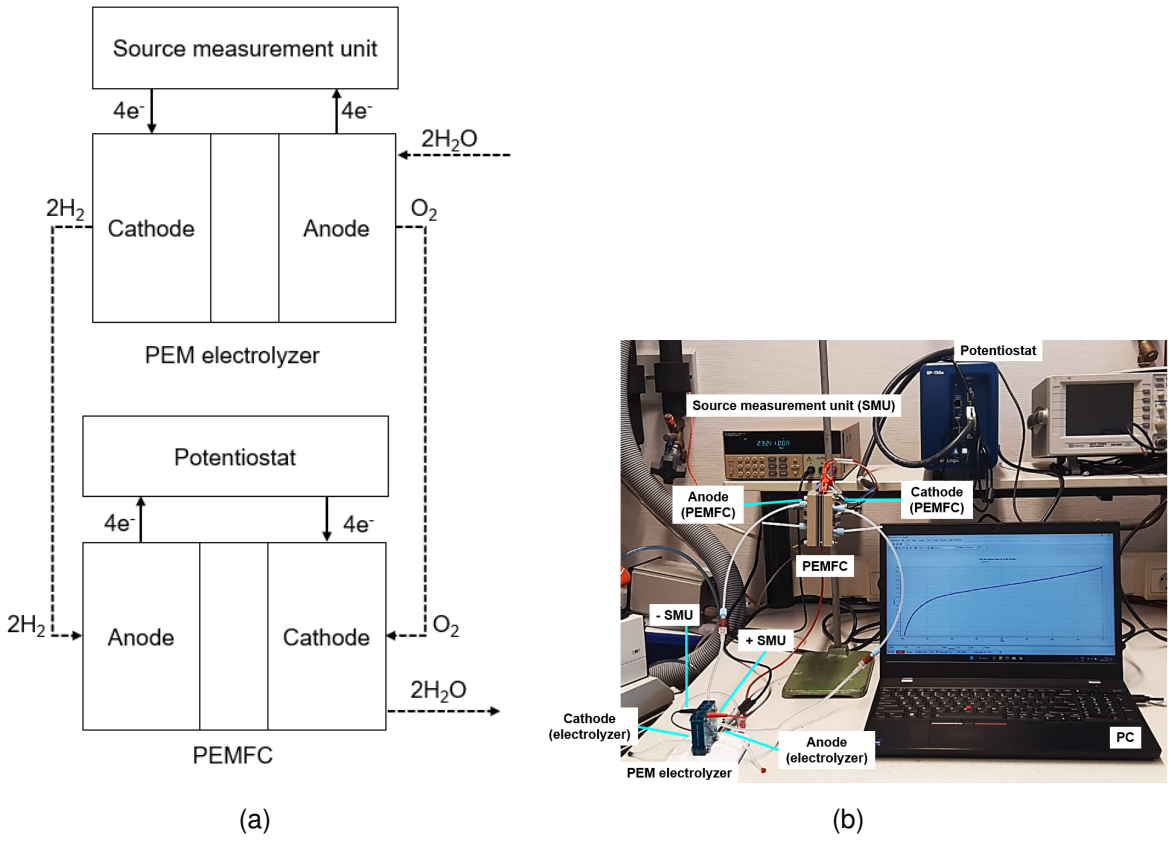

(a) (b)

Figure 3.2: (a) Schematic of the experimental setup. Operation of a PEMFC, characterised by a potentiostat. A PEM electrolyzer is used as the reactants (hydrogen and oxygen) supply unit, at rates controlled by a source measurement unit, (b) Experimental setup for operating a PEMFC.

Chapter 4

Research Methods

To study the load current-cell potential (I-E) characteristics of PEMFCs, the experimental procedure for assembling a PEM fuel cell, setting it up with the electrolyzer are presented, followed by different techniques for I-E characterisation. The procedure and techniques were constructed based on the settings used in literature [51], [52].

4.1 Experimental procedure

The following steps were followed for setting up a PEMFC:

4.1.1 Setting up the electrolyzer

1. The electrolyzer has two ports each on the anode and the cathode side. Deionized (DI) water was used to clean the electrolyzer and hydrate the respective membrane by flushing DI water through the ports.
2. On each side, one of the ports was closed to direct the flow of gases towards the PEMFC.
3. The connection between the cathode and anode of the electrolyzer to the negative and positive terminals of the source measurement unit were established respectively.
4. The electrolyzer current was set in the source measurement unit. A compliance of 3 V was set to prevent damaging the electrolyzer. Literature shows that the electrolyzer's electrodes oxidises for a potential greater than 3 V, which might reduce the life of the electrolyzer [53].

5. Excess water in the outlet tubes was flushed out before connecting them to the PEMFC.
6. The other ports on the cathode and anode side of the electrolyzer were connected to the PEMFC anode and cathode respectively.

4.1.2 Fuel cell preparation

1. The PEMFC components suited for the active area of a chosen MEA were selected and rinsed with DI water.
2. Components other than the MEA and the frame were assembled for anode and cathode side in the order: end plate, Viton gasket, current collector, FFP, and gaskets.
3. One half-cell was secured with four M3 bolts to hold the components in place.
4. The MEA and the frame were placed over one half-cell, followed by the placement of the other half-cell. The alignment of MEA's active area with the serpentine channels of the FFPs was ensured by visual inspection.
5. The PEMFC assembly is fastened with four M3 nuts with a torque of 0.3 N.mm.
6. The connections between the PEMFC and the potentiostat, and between the potentiostat and a personal computer (PC) were established. The working electrode and counter electrode (shorted to the reference electrode) of the potentiostat were connected to the cathode and anode current collector terminals of the PEMFC respectively.
7. A experiment protocol was formulated in EC-Lab® and the data (time, load current, cell potential, fuel cell output power) was recorded in the PC.
8. Before each experiment, the PEMFC was allowed to stabilise for 30 to 60 s at OCV.

The procedure was carried out for the three PEMFCs.

4.2 I-E characterisation of PEMFCs

To record the load current-cell potential (I-E) relation of a PEM fuel cell as seen in Chapter 2, each PEMFC was assembled and subjected to different electric loads, i.e., the PEMFC was used as a power source and the potentiostat was used as a variable electric load. The I-E characteristics of the PEMFCs were recorded in two ways.

Firstly, the **dynamic** response of the PEMFC was recorded with a linear sweep voltammogram. The cell was maintained at OCV for 60 s. Then the load current was increased from 0 mA at a rate of 5 mA.s^{-1} until the measured cell potential reached 0 V. The lower limit for the cell potential was set to 0 V to prevent cell reversal that could damage the fuel cell membrane [52]. Higher current scan rate and instantaneous measurement attributes to the dynamic characterisation. Three trials of experiments were carried out with PEMFC of each active area using this setting. The interpolated and averaged data from the trials is represented as experimental I-E data in the upcoming discussions.

In the second method, the **steady-state** cell potential of the PEMFC(s) was recorded at different load currents, with each load current maintained constant for a finite duration. The cell was maintained at OCV for 30 s followed by a sequence of increasing load currents applied in steps of 25 mA starting from 25 mA and maintained for 30 s. This was done until the cell potential dropped to 0 V.

Both these experiments were done using current-controlled techniques, and the measurement of cell potential was done every 0.1 s. The variations of load current and cell potential with time using these two settings are shown in Fig. 4.1.

4.3 Estimation of activation parameters from CV experiments

To estimate the activation parameters (transfer coefficient α and exchange current I_0) of each PEMFC, Cyclic Voltammetry (CV) experiments were carried out. Cyclic Voltammetry (CV) is an electrochemical technique that sweeps the voltage (cell potential) of the working electrode linearly with time and measures the load current. The sweeps are typically carried out in forward and backward directions (low voltage to high voltage and vice-versa) constituting one cycle. Multiple cycles were done to ensure repeatability and to identify the irreversibilities of the cell.

A CV experiment was performed on each PEMFC from 0.5 V to 0.9 V with scan

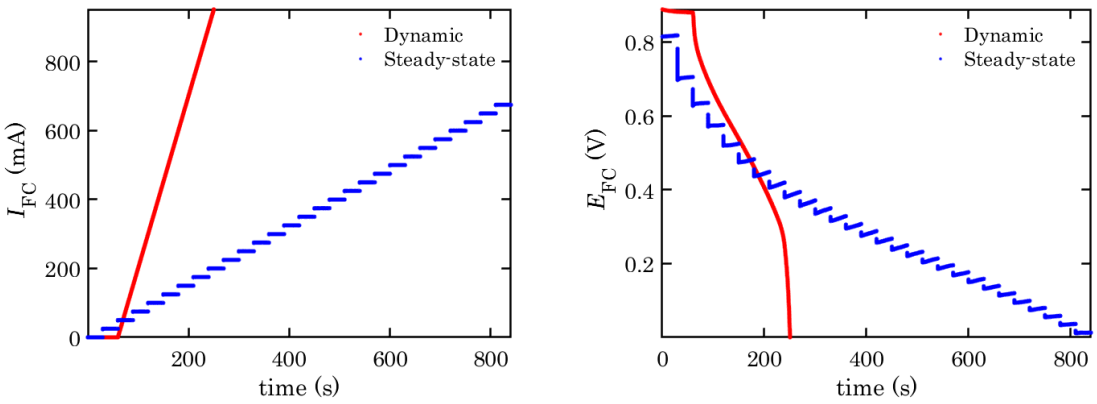

Figure 4.1: Dynamic and steady-state load setting with load current (controlled quantity) and cell potential (measured quantity) (a) time versus load current (b) time versus cell potential.

rates of 100 mV.s^{-1} and 20 mV.s^{-1} for 5 cycles. The averaged current was recorded over 10 voltage steps every 0.1 s. The upper threshold voltage was set to 0.9 V as it was higher than the recorded OCVs of all the PEMFCs, thereby providing more insight into the PEMFC's behavior in the low-load current region, where the activation overpotential is dominant. Typically, scan rates in the range of 1 to 100 [mV.s^{-1}] are used in CV experiments [54].

Tafel plot ($\log(I)$ versus E_{cell}) provides insight into the activation kinetics of an electrochemical system [23], [32]. By fitting a straight line (linear fitting) in a Tafel plot (Fig. 4.2), the activation parameters are found as follows,

$$\alpha = \frac{RT}{mF}, \tag{4.1}$$

$$I_0 = \frac{\alpha F}{RT} \exp(c - E_0), \tag{4.2}$$

where, m is the slope of the straight line, and c is the y-intercept of the straight line. The derivation of activation parameters and the linear fitting in Tafel plots for other PEMFCs for two different CV scan rates can be found in Appendix C.

4.4 Measurement of Ohmic resistance

The Ohmic loss in a fuel cell is proportional to the cell resistance, which is intuitive from Ohm's law. The uncompensated Ohmic drop between the cathode and anode terminals of the PEMFC was measured by recording the impedance response

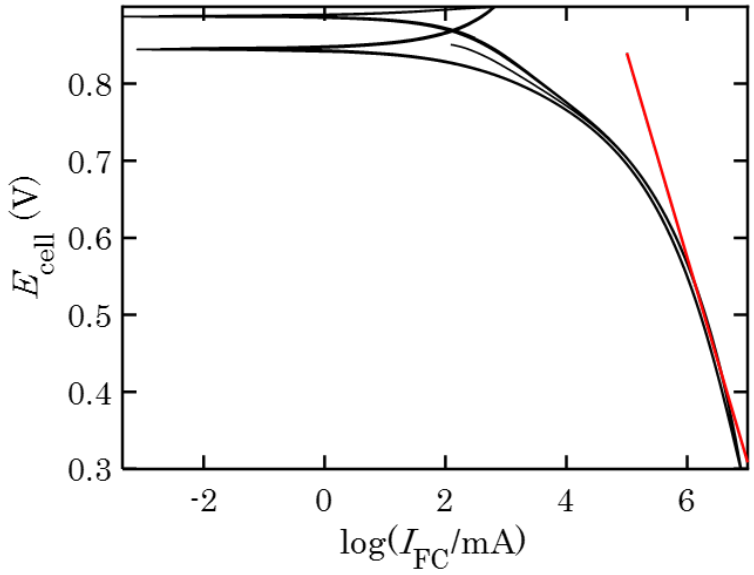

Figure 4.2: Linear fitting in a Tafel plot (active area: 3.5×3.5 cm^2, I_{EL} = 1 A, CV scan rate: 100 mV.s^{-1})

of the PEMFC by subjecting it to a high-frequency sine voltage (maximum voltage: 20 mV, frequency: 100 kHz) at OCV [55], [56]. The uncompensated resistance was considered as the Ohmic resistance of the PEMFC (R_{FC}) over the compensated resistance because the former takes into account the resistance between the PEMFC electrodes along with other parasitic resistances (such as resistance due to wire contacts and resistances of the PEMFC plates). This was done using ZIR technique provided in EC-Lab®,

The three PEMFCs were well hydrated and their cell resistances were recorded using the high-frequency impedance measurement technique described above. Too much hydration could cause flooding and too little hydration could lead to membrane dehydration and poor conductivity. Hence an optimum level of hydration is required [15]. The hydration level was ensured by the discharge of water from the outlet ports on each side of the PEMFC. Ten measurements were recorded for each PEMFC and the average was taken as R_{FC} with a maximum standard deviation of 0.25 Ω (Appendix D).

These experiments were performed to obtain the I-E or polarization characteristics to study the range of operating current, cell potential and power of the fuel cells under ambient conditions (295.12 K, atmospheric pressure of 1.01325 bar, relative humidity of 48 %).

Chapter 5

Discussions

The results of PEMFCs' characterisation and mathematical model are presented.

5.1 Estimation of activation and Ohmic parameters from CV and ZIR experiments

For the estimation of activation parameters from linear fitting in Tafel plots from the CV experiments, the I-E data obtained using a higher scan rate of 100 mV.s^{-1} is considered over a low CV scan rate 20 mV.s^{-1}. This is done because the active area of the membrane degrades when CV sweeps with long cycle duration and lower scan rates are used [57]. Therefore a higher scan rate of 100 mV.s^{-1} was used, which also ensured that the cell did not operate as an electrolyzer for a longer duration, which might degrade the membrane due to cell reversal [58]. The activation and Ohmic parameters estimated from the CV experiments using linear fitting in Tafel plots (with a scan rate of 100 mV.s^{-1}) and ZIR experiments are presented in Table. 5.1.

Table 5.1: Activation and Ohmic parameters from the CV and ZIR experiments.

MEA length [cm]	α **[non-units]**	I_0 **[mA]**	R_{FC} **[Ω]**
3.5	0.096	127.829	0.375
2.7	0.082	41.027	0.746
1.6	0.072	34.878	2.97

5.2 Effect of clamping torque on PEMFC performance

The PEMFCs were initially clamped using nylon fasteners with a clamping torque of 0.1 N.mm. It resulted in the nylon bolts slipping through the nylon nuts as it was not able to handle higher clamping torques. They were later replaced with stainless steel fasteners wrapped with Teflon tape, with a clamping torque of 0.3 N.mm.

It can be observed from Fig. 5.1 that the slope of the Ohmic region in the I-E plot for metal fasteners (solid line) is lower than that for nylon fasteners (dotted line). Therefore, it is evident that higher clamping torque enhances the fuel cell performance by making the internal path less resistive. This shows the importance of maintaining uniform clamping torque across the fuel cell assembly.

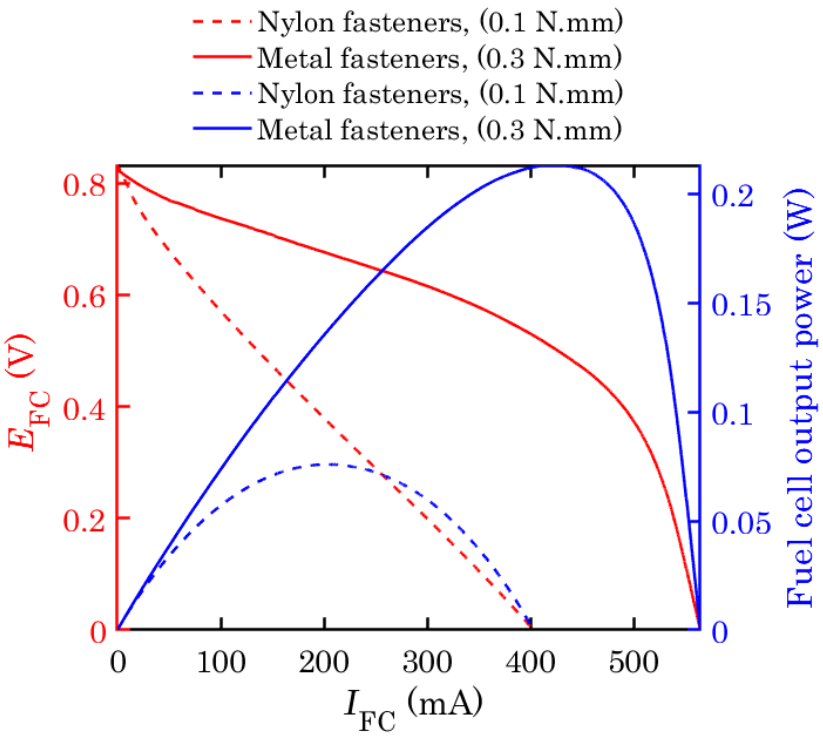

Figure 5.1: I-E characteristics of PEMFC of active area 3.5×3.5 cm^2 with I_{EL}=1 A, with Nylon fasteners clamped at 0.1 N.mm (dotted line) and metal fasteners wrapped in Teflon tape clamped at 0.3 N.mm (solid line).

The fuel cell operation was verified by the formation of water in the FFPs after the experiments (Fig. B.4). The water formed at the catalyst layer of the MEA as a result of the fuel cell redox reaction discharged through the gaps and can be seen in the FFPs.

5.3 Influence of oxygen source on PEMFC performance

The cathode reactant gas for the PEMFCs is oxygen, which could be supplied by the electrolyzer or derived from atmospheric air. It can be seen from Fig. 5.2 that the choice of oxygen source significantly affects the performance of the PEMFC in the high-load current region.

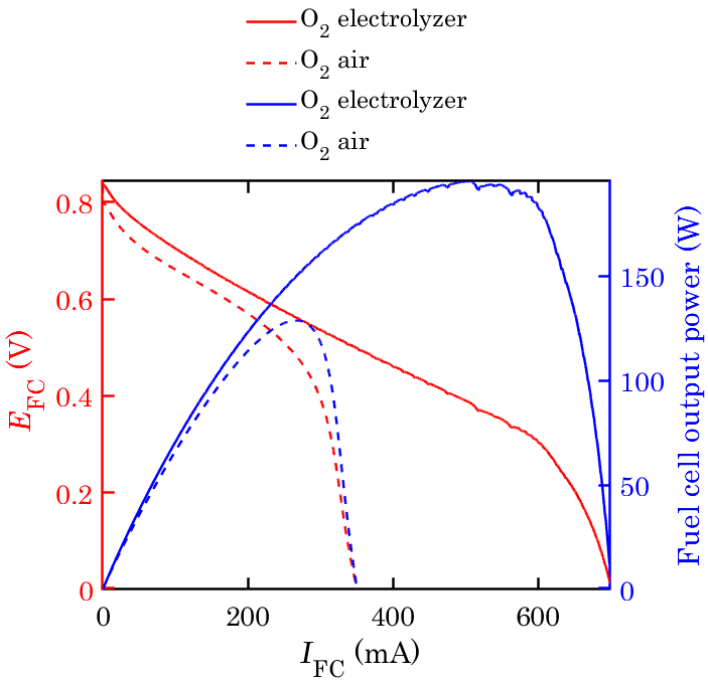

Figure 5.2: Comparison of PEMFC performance for oxygen from electrolyzer as cathode gas (solid line) versus oxygen from air as cathode gas (dotted line) (active area: 3.5×3.5 cm^2, I_{EL} = 1 A).

The partial pressure of oxygen (p_{O_2}) with air as cathode gas is $(0.21 \cdot P_{atm})$[1]. When oxygen is supplied from the electrolyzer, the expression for p_{O_2} becomes $(0.21 \cdot P_{atm}) + (0.5 \cdot p_{H_2})$ as the excess pressure at PEMFC cathode is also taken into account.

From Fig. 5.2, it can be seen that the OCV is almost the same for oxygen from electrolyzer and air. This implies that the partial pressures of hydrogen and oxygen are almost the same in both these cases, using Nernst equation (2.4).

[1] P_{atm} = 1 atm = 1.01325 bar.

$$\begin{aligned} & E_0(\text{O}_2 \text{ from electrolyzer}) \approx E_0(\text{O}_2 \text{ from air}) \\ \implies & p_{\text{O}_2}(\text{O}_2 \text{ from electrolyzer}) \approx p_{\text{O}_2}(\text{O}_2 \text{ from air}) \\ \implies & (0.21 \cdot P_{atm}) + (0.5 \cdot p_{H_2}) \approx 0.21 \cdot P_{atm} \end{aligned} \tag{5.1}$$

This also means that the partial pressure of hydrogen is negligible. The partial pressure of hydrogen was found for PEMFCs of different active areas using this consideration (5.1) and can be found in Appendix E.2.

In a mixture of gases, the partial pressure of a gas i is related to its concentration χ by the following relation,

$$p_i = \chi_i \cdot P_{\text{total}} \tag{5.2}$$

where, P_{total} is the total pressure of the mixture of gases.

There is a linear relation between the concentration of the gas and its partial pressure. Therefore, it can be inferred that the concentration of reactants in both cases is the same since their OCVs are approximately equal.

Fig. 5.2 also illustrates that the difference in PEMFC performance is significant in the polarization region where the concentration overpotential is dominant. As seen earlier, concentration loss occurs due to the rapid depletion of fuel cell reactants near the active areas of the membranes. With air as the cathode gas, the cathode was left open to the atmosphere and the hence flow rate of oxygen was zero. It can be seen that the flow rates of fuel cell reactants limit their performance. This is further elaborated in the upcoming discussion on the effect of flow rates on PEMFC performance (Section 5.4).

Literature also suggests that better fuel cell performance with reduced activation and concentration overpotentials was observed when oxygen from an exclusive oxygen source than oxygen from air [32], [42], [59].

In the subsequent discussions, oxygen from the electrolyzer is supplied to the PEMFC cathode.

5.4 Effect of reactant flow rates on PEMFC performance

As seen in Section. 4.2, three experimental trials were performed with the same dynamic settings and the mean load current, cell potential and output power were plotted, with the error bars representing 1 standard deviation about the mean load current.

The activation kinetics and Ohmic resistance are intrinsic to a PEMFC, i.e., they depend on the geometry and material properties of the cell. They are unaffected by the reactants' flow rate, represented by the electrolyzer current. The OCV or no-load cell potential is unaffected by different reactant flow rates (Appendix E.1). Fig. 5.3 (a) demonstrates the change in electrolyzer current, which represents the flow rates of reactants from Faraday's law of electrolysis (equation 3.4), affects the concentration overpotential and not the activation or Ohmic overpotentials.

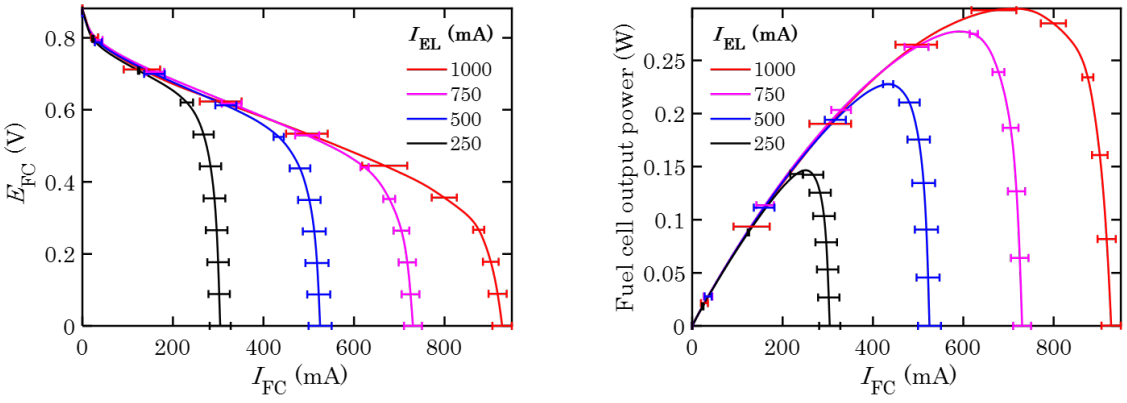

Figure 5.3: (a) I-E characteristics of PEMFC, and (b) load current versus output power of PEMFC (active area: 3.5×3.5 cm^2) for different electrolyzer currents I_{EL} = 1000, 750, 500, and 250 [mA].

It is also in agreement with the fact that any fuel cell cannot operate at rates[2] higher than the supply rates from the electrolyzer. The electrolyzer current (I_{EL}) restricts the maximum operating current of the fuel cell represented by the fuel cell's limiting current, (I_L). Therefore a linear relation between the electrolyzer current (controlled quantity) and the PEMFC limiting current (measured quantity) can be observed (Fig. 5.4). However, in these experiments, the PEMFC load currents were

[2]Here, rates refer to both the current and rate of reactants flow, since both these terms are linearly dependent.

varied dynamically. Hence the fuel cell appears to outperform the electrolyzer as the measurements were recorded instantaneously.

Operating PEMFCs with higher reactant flow rates yields higher output power, as also verified in the literature [60]. Operating the PEMFC with higher reactant flow rates can be used to drive electric loads with large current requirements (Fig. 5.3 (b)).

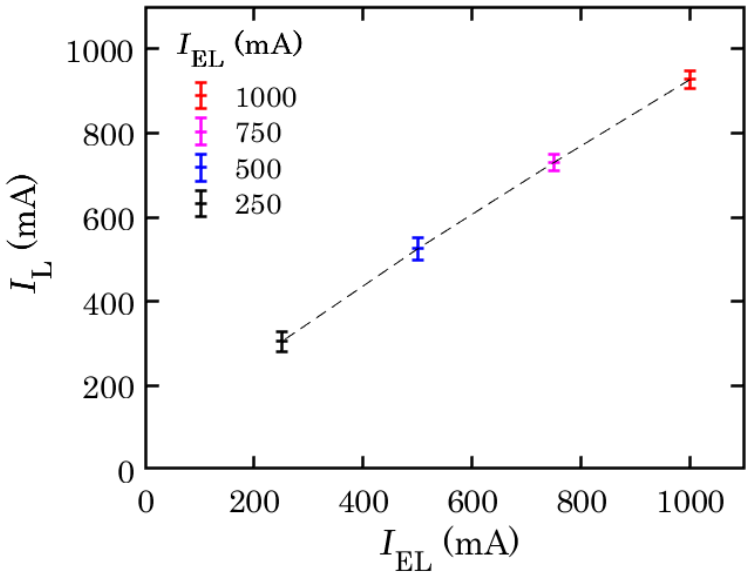

Figure 5.4: Linear relation between the electrolyzer current (I_{EL}) and the PEMFC limiting current (I_L) (active area: 3.5×3.5 cm^2).

5.5 Effect of MEA's active area on PEMFC performance

The relation between activation parameters (transfer coefficient and exchange current) and active area of the fuel cell membrane is first analysed. There is no explicit relation between the transfer coefficient and the active area of MEA [12], [61]. The exchange current is proportional to the catalyst's specific area which in turn is proportional to the active area of PEMFC [12], [32], [61]. The mentioned literature suggests that reducing the active area of PEMFCs results in a decrease in exchange current, thereby increasing the activation overpotential and decreasing the overall cell potential (equation 2.15).

From Fig. 5.5 it can be seen that the slope of the linear region in the I-E characteristics increases with a decrease in MEA active area[3]. This is intuitive, as a decrease in the active area of PEMFCs does increase the resistance of the membrane while maintaining its thickness and resistivity constant. Membrane resistance is inversely proportional to its area, provided membrane thickness and resistivity are constant. This contributes to an increase in the Ohmic overpotential.

From the above two reasons, down-scaling of PEMFCs leads to an increase in the activation and Ohmic overpotentials, thereby reducing the overall cell potential and limiting the cell performance (Fig. 5.5). This inference is in agreement with the results from the CV and ZIR experiments (Table 5.1).

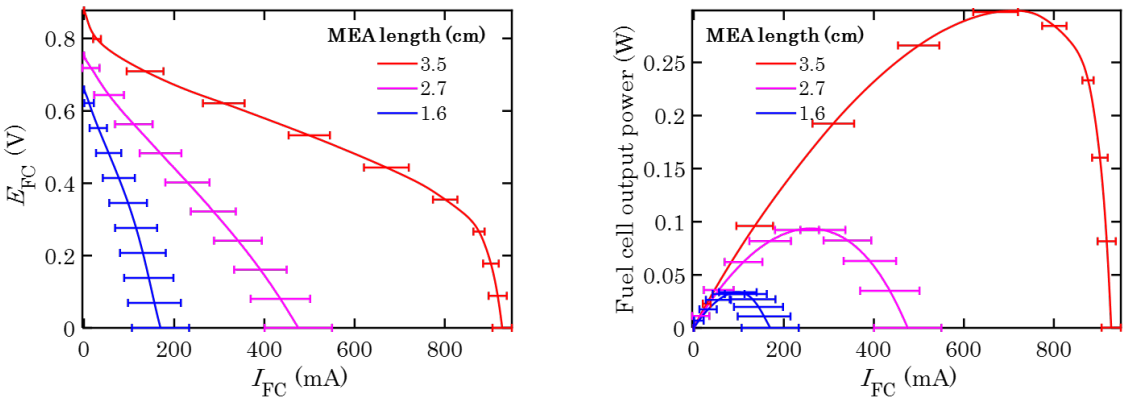

Figure 5.5: (a) I-E characteristics, and (b) output power of PEMFCs of different active areas: 3.5×3.5 cm^2, 2.7×2.7 cm^2, and 1.6×1.6 cm^2 for I_{EL}=1 A.

[3]The MEA active area is represented by the square length of the MEA.

5.6 Comparison between dynamic loading and steady-state loading

In the above discussions, the PEMFCs were subjected to dynamic loads. To compare dynamic I-E characterisation with steady-state I-E characterisation, the PEMFCs' cell potentials were recorded dynamically and in steady-state (Section 4.2).

For dynamic measurements, since the cell potential was recorded instantaneously, there is a one-to-one relation between the load current and cell potential. The dynamic response of the cell is useful to analyse the cell's performance when it is subjected to sudden changes in load current, such as a high-frequency oscillator. Measurement of cell potentials in the transient state implies that the I-E characteristics do not reflect the true behavior of the cell.

The steady-state experiment gives insight into the fuel cell operation for static loads, where the current drawn does not vary with time. When the cell operates in steady-state, the transient nature of the cell is absent, therefore, the cell's operation is closer to its true operation in terms of response time, current-potential relation, and settling time. It can be seen from Fig. 4.1 (b) that the steady-state cell potential continues to increase over a span of 30 s. This suggests that a settling time of more than 30 s could capture the steady-state response of the PEMFCs better.

The difference between these two settings is tied to the dwell time assigned to the measurement of cell potential.

Figures 5.6 and 5.7 compare the dynamic and steady-state loading for the three PEMFCs, with their steady-state current and voltage data point indicated in blue circles. The dynamic and steady-state performances are comparable for PEMFCs of smaller active areas, while there is a significant difference for the largest PEMFC. Literature shows that a fuel cell can be modelled using resistive and capacitive components as an RC system [62], [63]. These results could hint that there is a relation between the fuel cell's active area and its time constant.

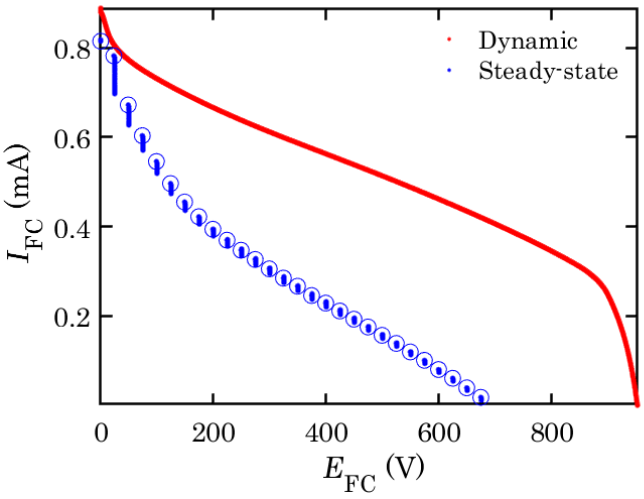

Figure 5.6: Dynamic and steady-state I-E characteristics of PEMFC (active area: 3.5×3.5 cm^2, I_{EL}=1A)

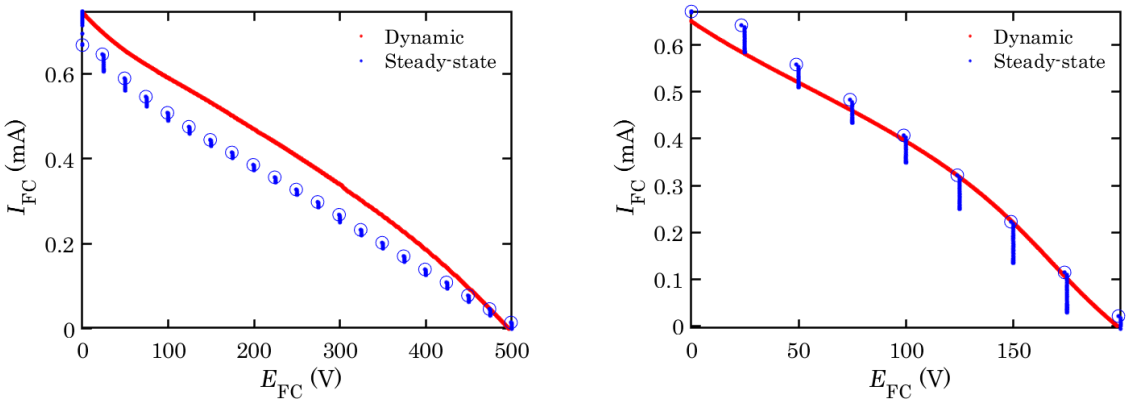

Figure 5.7: Dynamic and steady-state I-E characteristics of PEMFC (a) active area: 2.7×2.7 cm^2, I_{EL}=1A (b) active area: 1.6×1.6 cm^2, I_{EL}=1A

5.7 Semi-empirical mathematical modelling of PEMFC

The objective is to validate the experiments and understand the activation kinetics of the PEM fuel cell. Ohmic resistance measured from the ZIR experiments was used as R_{FC} for Ohmic overpotential (equation 2.22). Limiting current was taken as the maximum fuel cell load current for calculating the concentration overpotential (equation 2.23). Based on this equation, the concentration overpotential becomes infinity at the last data point of load current (at $I_{\mathrm{FC}} = I_L$). Hence the last data point of concentration overpotential was taken as its previous data point. The relation between the fuel cell load current and cell potential is used as the governing equation. Equation 2.24 was used as the governing equation.

The activation parameters were estimated semi-empirically using three approaches as explained below and are given in Table. 5.2.

1. The activation parameters were estimated from linear fitting in Tafel plots obtained from Cyclic Voltammetry experiments performed at a scan rate of 100 mV.s^{-1} (Sections 4.3, 5.1).
2. Genetic algorithm was used (population size: 500, maximum number of generations: 500) to fit experimental I-E characteristics with the governing equation to estimate the activation parameters.
3. Non-linear least squares fit was to fit the experimental I-E characteristics with the characteristic equation to estimate the activation parameters.

The estimated activation parameters were used in the governing equation to estimate the cell potential. The estimated I-E characteristics were compared with those from experiments (Fig. 5.8).

Table 5.2: Activation parameters estimated from 3 semi-empirical maethods.

Estimation method	α **[no-units]**	I_0 **[mA]**
Linear fitting in Tafel plot	0.096	127.829
Genetic algorithm	0.608	21.814
Nonlinear fit	1.682	0.055

The primary objective of modelling is to mathematically correlate the fuel cell parameters (activation parameters and resistance) with the experimental I-E characteristics. The purpose of modelling is specific to the application such as diagnostics,

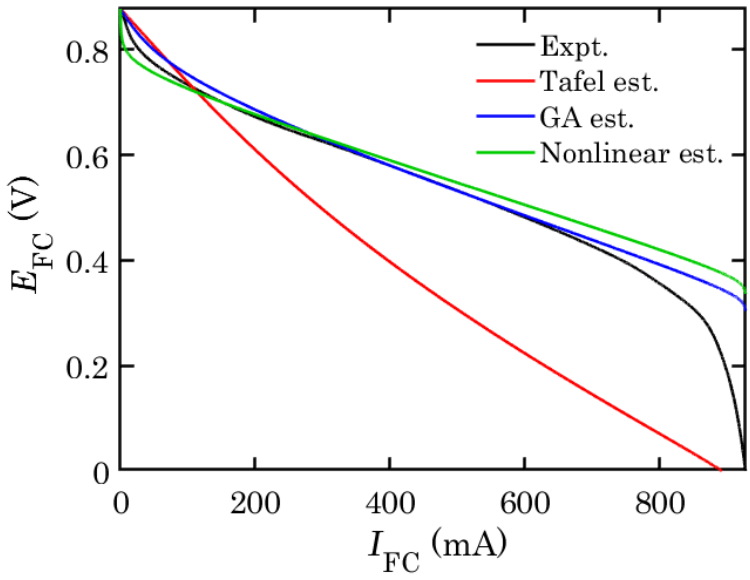

Figure 5.8: Validation of I-E characteristics of PEMFC (active area: 3.5×3.5 cm^2, I_{EL} = 1 A) with models using activation parameters estimated from linear fitting in Tafel plot, genetic algorithm and nonlinear estimation.

simulation and prediction of PEMFC performance. The goal of mathematical modelling in this study is to get insights into the activation kinetics of the PEM fuel cells.

Multiple models such as static and dynamic models have been proposed based on the experimental setup and control parameters such as temperature, pressure, concentration and humidity of reactant gases [64]. In this study, since there was a direct connection between the reactants supply unit (the electrolyzer) and the PEMFC(s) without any control over temperature, pressure or humidity, a simple model using the I-E relation for a fuel cell is used (equation 2.24).

Literature shows that experimental data have been used to estimate parameters (such as diffusion coefficient and activation parameters) semi-empirically using numerical methods. Such estimated parameters are useful to understand the internal kinetics and electrochemical aspects of the fuel cell [28], [65]. Shen [30] used genetic algorithm to estimate the activation parameters by fitting experimental I-E data from PEM fuel cells. Touré [66] used Lagrange's multiplier method to estimate the transfer coefficient.

It is apparent from Fig. 5.8 that the model obtained using activation parameters from Tafel plots has the poorest fit. The inaccuracy stems from the linear fitting as there is no definite Tafel regime and by arbitrarily fitting a straight line in the Tafel plot [67]. Models using activation parameters estimated using genetic algorithm and nonlinear least squares fit provide a good fit in the activation and Ohmic regions.

While the range of exchange current is unique to a fuel cell, the transfer coefficient is said to range from 0 to 1 [12]. Therefore the activation parameters estimated from genetic algorithm could be closer to the actual values since the transfer coefficient falls within the specified range and the model captures the activation kinetics better. Although the models using gentic algorithm and nonlinear fit seem to capture the activation and Ohmic behavior of the fuel cell, the models fall short in capturing the mass-transport or concentration behavior of the cell. Previous works that have used mathematical models to validate their experiments (or vice-versa) have also reported their models that did not capture the behavior of the fuel cell in such high load-current region [14], [68]. It might be helpful to use an exponential expression instead of a logarithmic one for computing the concentration overpotential as done by Kim *et al.* [68].

While literature provides physical meaning and ranges for parameters of a system, numerical methods can be used for parameter estimation. The results can be cross-verified with those obtained from dedicated experiments, such as linear fitting in Tafel plot, to compare the accuracies of the methods. These results could be used for further investigation of the activation kinetics of the fuel cells. In this study, a simple model using the I-E relation for a fuel cell was used for the model. Perhaps a dynamic model that considers the fuel cell parameters as time-dependent variables could be used for more accurate modelling.

5.8 Impedance matching with an electric load

To assess the transduction of electric power, an inductor coil (rated current: 130 mA, winding resistance: 8 Ω, rated inductance: 150 mH) was connected to the smallest PEMFC (active area: 1.6×1.6 cm^2). The voltage in an inductor is given by the following equation:

$$V_L = L\frac{\mathrm{d}I}{\mathrm{d}t} + R_L I, \tag{5.3}$$

where the term $(L \cdot \mathrm{d}I/\mathrm{d}t)$ represents the inductive behavior, and $(R_L \cdot I)$ represents the Ohmic behavior from the winding resistance of the inductor coil [Ω] (R_L). The observed I-E characteristics are illustrated in Fig. 5.9.

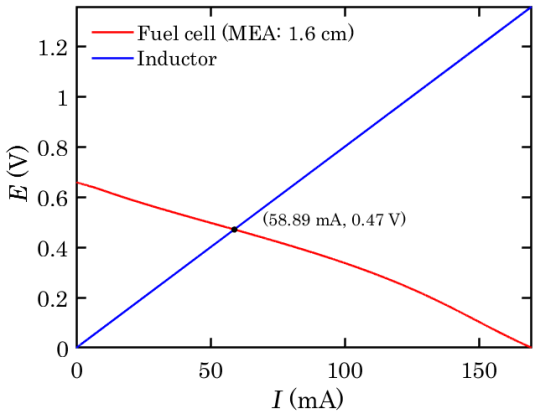

Figure 5.9: Operating point of electric load (inductor coil) from the I-E characteristics of PEMFC (active area: 1.6×1.6 cm^2, I_EL = 1 A) and inductor coil (rated 130 mA, 8 Ω, 150 mH).

From the voltage equation of an inductor coil (5.3), there is a DC voltage component that represents the voltage drop due to winding resistance. There is an Alternating Current (AC) voltage component that depends on the time-varying current. With the PEMFC connected directly to the coil, there is no time-varying current, i.e., current drawn by the coil is DC. This indicates that the coil behaves as a resistor. This characteristics provides insight into the use of the PEMFC as a DC electric source within a voltage range of up to 0.65 V. To achieve time-varying current through the coil for periodic oscillations in autonomous applications, an intermediate oscillator circuit could be introduced between the PEMFC (electric power source) and the coil (load).

Chapter 6

Conclusions

PEM fuel cells (PEMFCs) of active areas 3.5×3.5, 2.7×2.7, and 1.6×1.6 [cm^2] were designed and operated under different load conditions. The following conclusions were drawn to answer the research questions posed in Section 1.2.

1. **Can a single-cell PEMFC be used as an onboard power source for an autonomous device?**
   The use of PEMFCs as a DC power source was verified with a maximum output power of 0.3, 0.09, and 0.03 [W] (maximum power densities of 0.0245, 0.0123, and 0.0117 [$W.cm^{-2}$]) with descending order of PEMFC active area respectively. The use of a PEMFC as a power source for an application depends on the power requirements of the electric load. In this case, the use of the smallest PEMFC as a DC power source was verified by observing the resistive behavior of an inductor coil at 0.0277 W (0.0108 $W.cm^{-2}$).

2. **In relation to the requirement of downscaling onboard power sources for an autonomous device, how does the reduction in the active area of the PEM fuel cells affect their performance?**
   With the reduction in the PEMFCs' active area, the performance decreases due to an increase in activation and Ohmic losses that depend on the active area. Parasitic losses such as leakage, non-uniform compression, and contact resistances are more pronounced with the reduction in PEMFC active area. The drop in OCV as the active areas decrease can be attributed to lower reactants' partial pressures due to leakage.

3. **What are the challenges involved in operating PEM fuel cells?**
   For a single PEM fuel cell, an OCV less than 0.9 V can be attributed to leakage in the delivery of the reactants to the PEMFC and insufficient reactants supply [12]. For the setup devised, the partial pressures of reactants could vary during

the PEMFC loading, which could lead to variable OCV during loading. The fuel cell efficiency varies linearly with the cell potential (equation 2.27, Appendix F). It gives insight into the thermal losses when the PEMFC is loaded. Enhanced fuel cell performance with higher reactant flow rates was verified.

Chapter 7

Recommendations

Using a pressure-controlling valve to supply reactants at a constant pressure could improve the repeatability of PEMFC operation. Since hydrogen is very susceptible to leakage, the setup should be improved to minimise leakages. The parasitic losses that reduce the cell performance could be minimised by improving the assembly setup, such as membrane hydration before loading, supplying reactants at a higher rate and higher concentrations, reducing tube lengths, and replacing the current fasteners. The metal fasteners with Teflon tape wrapped around them could create non-uniform compression across the assembly based on the wrapping. Operating the PEMFC at high pressure, temperature, and humidification temperatures could enhance the PEMFC performance.

For the long-term goal of using a PEM fuel cell as an onboard power source for a magnetically actuated device, an electronic circuit is required to bridge the fuel cell to an inductor coil. The circuit should be able to generate a time-varying current to generate a time-varying magnetic dipole moment. The power requirements of the circuit should be matched with that of the fuel cell using impedance matching. A single-cell PEMFC cannot deliver a voltage greater than 1.229 V at ambient temperature and pressure. If the electric power demand from the circuit and the load (coil) is greater than that supplied by the PEMFC, a series of cells constituting a PEM fuel cell stack could be used as an onboard power source (Fig. 7.1). While designing such a fuel cell stack, it is important to consider the thermal loss in the stack and mass of the onboard system. Designing the current collectors with holes is one recommendation to reduce the mass of the fuel cell stack.

While designing the oscillator circuit, the current through the coil should have positive and negative half-cycles for continuous back-and-forth turning about one axis. The transition time between one operating current to another will determine the speed of rotation. The signal parameters should be fixed based on the desired

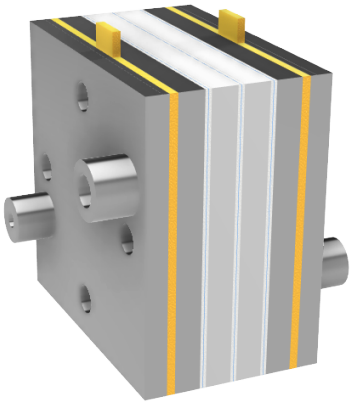

Figure 7.1: Design of PEM fuel cell stack (3 cells) in Fusion 360.

operation: frequency, rate of change in current, and signal profile. The load operation could be simulated using the potentiostat. The generated torque should be able to turn the entire capsule. Therefore, a preliminary torque-balance calculation is required for the selection of a coil, capsule design, and manoeuvrability of the device.

Bibliography

[1] J. D. Bjerknes, W. Liu, A. F. Winfield, C. Melhuish, and C. Lane, "Low cost ultrasonic positioning system for mobile robots", *Proceeding of Towards Autonomous Robotic Systems*, pp. 107–114, 2007.

[2] F. R. Stewart, Y. Qiu, H. S. Lay, *et al.*, "Acoustic sensing and ultrasonic drug delivery in multimodal theranostic capsule endoscopy", *Sensors*, vol. 17, no. 7, p. 1553, 2017.

[3] M. E. Alshafeei, A. Hosney, A. Klingner, S. Misra, and I. S. M. Khalil, "Magnetic-based motion control of a helical robot using two synchronized rotating dipole fields", in *5th IEEE RAS/EMBS International Conference on Biomedical Robotics and Biomechatronics*, 2014, pp. 151–156. DOI: 10.1109/BIOROB.2014.6913768.

[4] M. R. Basar, F. Malek, K. M. Juni, M. S. Idris, M. I. M. Saleh, *et al.*, "Ingestible wireless capsule technology: A review of development and future indication", *International Journal of Antennas and Propagation*, vol. 2012, 2012.

[5] M. A. Al-Rawhani, J. Beeley, and D. R. Cumming, "Wireless fluorescence capsule for endoscopy using single photon-based detection", *Scientific reports*, vol. 5, no. 1, p. 18 591, 2015.

[6] W. Andre and S. Martel, "Design of photovoltaic cells to power control electronics embedded in untethered aqueous microrobots propelled by bacteria", in *2006 IEEE/RSJ International Conference on Intelligent Robots and Systems*, IEEE, 2006, pp. 1335–1340.

[7] F. Bianchi, A. Masaracchia, E. Shojaei Barjuei, *et al.*, "Localization strategies for robotic endoscopic capsules: a review", *Expert review of medical devices*, vol. 16, no. 5, pp. 381–403, 2019.

[8] D. Jang, J. Jeong, H. Song, and S. K. Chung, "Targeted drug delivery technology using untethered microrobots: A review", *Journal of Micromechanics and Microengineering*, vol. 29, no. 5, p. 053 002, 2019.

[9] A. W. Mahoney and J. J. Abbott, “Generating rotating magnetic fields with a single permanent magnet for propulsion of untethered magnetic devices in a lumen”, *IEEE Transactions on Robotics*, vol. 30, no. 2, pp. 411–420, 2013.

[10] S. Hosseini, M. Mehrtash, and M. B. Khamesee, “Design, fabrication and control of a magnetic capsule-robot for the human esophagus”, *Microsystem technologies*, vol. 17, pp. 1145–1152, 2011.

[11] G. Kosa, P. Jakab, F. Jolesz, and N. Hata, “B0-field-driven capsule endoscope with swimming tails for propulsion: design study”, in *Proc. Intl. Soc. Mag. Reson. Med*, 2007, p. 1106.

[12] C. Spiegel *et al.*, *Designing and building fuel cells*. Mcgraw-hill New York, 2007, vol. 87.

[13] M. M. Tellez-Cruz, J. Escorihuela, O. Solorza-Feria, and V. Compañ, “Proton Exchange Membrane Fuel Cells (PEMFCs): Advances and Challenges”, *Polymers*, vol. 13, no. 18, 2021, ISSN: 2073-4360. DOI: 10.3390/polym13183064. [Online]. Available: https://www.mdpi.com/2073-4360/13/18/3064.

[14] L. Wang, A. Husar, T. Zhou, and H. Liu, “A parametric study of PEM fuel cell performances”, *International journal of hydrogen energy*, vol. 28, no. 11, pp. 1263–1272, 2003.

[15] H. Sun, G. Zhang, L. Guo, and H. Liu, “A Study of dynamic characteristics of PEM fuel cells by measuring local currents”, *International journal of hydrogen energy*, vol. 34, no. 13, pp. 5529–5536, 2009.

[16] J. Artal, J. Dominguez, and J. Caraballo, “Autonomous Mobile Robot with Hybrid PEM Fuel-Cell and Ultracapacitors Energy System, Dedalo 2.0”, in *International Conference on Renewable Energies and Power Quality, Santiago de Compostela, Spain*, 2012, pp. 1–6.

[17] A. Wilhelm, B. Surgenor, and J. Pharoah, “Evaluation of a micro fuel cell as applied to a mobile robot”, in *IEEE International Conference Mechatronics and Automation, 2005*, IEEE, vol. 1, 2005, pp. 32–36.

[18] J. B. Siegel, Y. Wang, A. G. Stefanopoulou, and B. A. McCain, “Comparison of SOFC and PEM fuel cell hybrid power management strategies for mobile robots”, in *2015 IEEE Vehicle Power and Propulsion Conference (VPPC)*, IEEE, 2015, pp. 1–6.

[19] J. Thangavelautham, D. Strawser, M. Y. Cheung, and S. Dubowsky, “Lithium hydride powered PEM fuel cells for long-duration small mobile robotic missions”, in *2012 IEEE International Conference on Robotics and Automation*, IEEE, 2012, pp. 415–422.

[20] E. van Renselaar, B. Keitel, M. Dinc, *et al.*, “Scaling rules for microrobots with full energetic autonomy”, in *2022 International Conference on Manipulation, Automation and Robotics at Small Scales (MARSS)*, IEEE, 2022, pp. 1–6.

[21] S. B. Kesner, J.-S. Plante, P. J. Boston, T. Fabian, and S. Dubowsky, “Mobility and power feasibility of a microbot team system for extraterrestrial cave exploration”, in *Proceedings 2007 IEEE International Conference on Robotics and Automation*, IEEE, 2007, pp. 4893–4898.

[22] P. C. Hallenbeck, M. Abo-Hashesh, and D. Ghosh, “Strategies for improving biological hydrogen production”, *Bioresource technology*, vol. 110, pp. 1–9, 2012.

[23] D. Das and T. N. Veziroglu, “Advances in biological hydrogen production processes”, *International journal of hydrogen energy*, vol. 33, no. 21, pp. 6046–6057, 2008.

[24] S. Tanisho and Y. Ishiwata, “Continuous hydrogen production from molasses by the bacterium Enterobacter aerogenes”, *International Journal of Hydrogen Energy*, vol. 19, no. 10, pp. 807–812, 1994.

[25] N. Kataoka, A. Miya, and K. Kiriyama, “Studies on hydrogen production by continuous culture system of hydrogen-producing anaerobic bacteria”, *Water Science and Technology*, vol. 36, no. 6-7, pp. 41–47, 1997.

[26] S. Wilkinson, ““Gastrobots”—benefits and challenges of microbial fuel cells in foodpowered robot applications”, *Autonomous Robots*, vol. 9, pp. 99–111, 2000.

[27] I. Mills *et al.*, *Quantities, units and symbols in physical chemistry/prepared for publication by Ian Mills...[et al.]* Oxford; Boston: Blackwell Science; Boca Raton, Fla.: CRC Press [distributor], 1993.

[28] S. Haji, “Analytical modeling of PEM fuel cell i–V curve”, *Renewable Energy*, vol. 36, no. 2, pp. 451–458, 2011.

[29] I. Pilatowsky, R. J. Romero, C. Isaza, *et al.*, *Cogeneration Fuel Cells–Air Conditioning Systems*. Springer, 2011.

[30] J. Shen, C. Du, F. Yan, B. Chen, and Z. Tu, “Two parameters identification for polarization curve fitting of PEMFC based on genetic algorithm”, *International Journal of Energy Research*, vol. 46, no. 7, pp. 9621–9633, 2022.

[31] V. B. Silva and A. Rouboa, “Hydrogen-fed PEMFC: Overvoltage analysis during an activation procedure”, *Journal of Electroanalytical Chemistry*, vol. 671, pp. 58–66, 2012.

[32] P. K. Das, X. Li, and Z.-S. Liu, "Analytical approach to polymer electrolyte membrane fuel cell performance and optimization", *Journal of Electroanalytical Chemistry*, vol. 604, no. 2, pp. 72–90, 2007.

[33] E. J. Dickinson and G. Hinds, "The Butler-Volmer equation for polymer electrolyte membrane fuel cell (PEMFC) electrode kinetics: A critical discussion", *Journal of the electrochemical society*, vol. 166, no. 4, F221, 2019.

[34] M. Pan, C. Li, J. Liao, *et al.*, "Design and modeling of PEM fuel cell based on different flow fields", *Energy*, vol. 207, p. 118 331, 2020.

[35] S. Chugh, C. Chaudhari, K. Sonkar, A. Sharma, G. Kapur, and S. Ramakumar, "Experimental and modelling studies of low temperature PEMFC performance", *international journal of hydrogen energy*, vol. 45, no. 15, pp. 8866–8874, 2020.

[36] J. Larminie, "Fuel Cell Systems Explained", *JOHN WILEY & SONS. LTD google schola*, vol. 2, pp. 1324–1332, 2003.

[37] C. K. Jin, J. H. Kim, and B.-S. Lee, "Powder Bed Fusion 3D Printing and Performance of Stainless-Steel Bipolar Plate with Rectangular Microchannels and Microribs", *Energies*, vol. 15, no. 22, p. 8463, 2022.

[38] "Permeation resistance of poly (ether ether ketone) to hydrogen, nitrogen, and oxygen gases, author=Monson, Loxie and Moon, Sung In and Extrand, CW", *Journal of applied polymer science*, vol. 127, no. 3, pp. 1637–1642, 2013.

[39] R. R. Barth, K. L. Simmons, and C. W. San Marchi, "Polymers for hydrogen infrastructure and vehicle fuel systems", Sandia National Lab.(SNL-CA), Livermore, CA (United States); Pacific . . ., Tech. Rep., 2013.

[40] Y. Song, C. Zhang, C.-Y. Ling, *et al.*, "Review on current research of materials, fabrication and application for bipolar plate in proton exchange membrane fuel cell", *International Journal of Hydrogen Energy*, vol. 45, no. 54, pp. 29 832–29 847, 2020.

[41] K. H. Kim, J. W. Lim, M. Kim, *et al.*, "Development of carbon fabric/graphite hybrid bipolar plate for PEMFC", *Composite Structures*, vol. 98, pp. 103–110, 2013.

[42] A. Iranzo, P. Boillat, A. Salva, and J. Biesdorf, "PEM fuel cell operation under air and O2 feed: analysis of cell performance and liquid water distributions", *Fuel Cells*, vol. 16, no. 4, pp. 463–468, 2016.

[43] T. Wilberforce, Z. El Hassan, E. Ogungbemi, *et al.*, "A comprehensive study of the effect of bipolar plate (BP) geometry design on the performance of proton exchange membrane (PEM) fuel cells", *Renewable and sustainable energy reviews*, vol. 111, pp. 236–260, 2019.

[44] X. Li and I. Sabir, "Review of bipolar plates in PEM fuel cells: Flow-field designs", *International journal of hydrogen energy*, vol. 30, no. 4, pp. 359–371, 2005.

[45] M. Mortada, H. S. Ramadan, J. Faraj, A. Faraj, H. El Hage, and M. Khaled, "Impacts of reactant flow nonuniformity on fuel cell performance and scaling-up: Comprehensive review, critical analysis and potential recommendations", *International Journal of Hydrogen Energy*, vol. 46, no. 63, pp. 32 161–32 191, 2021.

[46] M. D. Lukas, K. Y. Lee, and H. Ghezel-Ayagh, "Development of a stack simulation model for control study on direct reforming molten carbonate fuel cell power plant", *IEEE Transactions on Energy Conversion*, vol. 14, no. 4, pp. 1651–1657, 1999.

[47] S. Asghari, A. Mokmeli, and M. Samavati, "Study of PEM fuel cell performance by electrochemical impedance spectroscopy", *International Journal of Hydrogen Energy*, vol. 35, no. 17, pp. 9283–9290, 2010.

[48] N. Ul Hassan, M. Kilic, E. Okumus, B. Tunaboylu, and A. Murat Soydan, "Experimental determination of optimal clamping torque for AB-PEM fuel cell", *Journal of Electrochemical Science and Engineering*, vol. 6, no. 1, pp. 9–16, 2016.

[49] A. Bates, S. Mukherjee, S. Hwang, *et al.*, "Simulation and experimental analysis of the clamping pressure distribution in a PEM fuel cell stack", *International journal of hydrogen energy*, vol. 38, no. 15, pp. 6481–6493, 2013.

[50] T. J. Mason, J. Millichamp, T. P. Neville, A. El-Kharouf, B. G. Pollet, and D. J. Brett, "Effect of clamping pressure on ohmic resistance and compression of gas diffusion layers for polymer electrolyte fuel cells", *Journal of Power Sources*, vol. 219, pp. 52–59, 2012.

[51] F. S. E. Center, "Procedure for performing PEM single cell testing", *Test Protocol for Cell Performance Tests Performed Under DOE Contract# DE-FC36-06G016028. vol. DOE# DE-FC36-06G016028. US Department of Energy, Arlington, Virginia*, 2009.

[52] G. De Marco, A. Pilenga, M. Honselaar, *et al.*, "Testing the Voltage and Power as Function of Current Density: Polarisation Curve for a SOFC Single Cell", *JRC: Petten, The Netherlands*, 2010.

[53] A. W. Tricker, T. Y. Ertugrul, J. K. Lee, *et al.*, "Pathways toward efficient and durable anion exchange membrane water electrolyzers enabled by electroactive porous transport layers", *Advanced Energy Materials*, p. 2 303 629, 2023.

[54] S. Prass, J. St-Pierre, M. Klingele, K. A. Friedrich, and N. Zamel, "Hydrogen oxidation artifact during platinum oxide reduction in cyclic voltammetry analysis of low-loaded PEMFC electrodes", *Electrocatalysis*, vol. 12, pp. 45–55, 2021.

[55] K. Cooper and M. Smith, "Electrical test methods for on-line fuel cell ohmic resistance measurement", *Journal of Power Sources*, vol. 160, no. 2, pp. 1088–1095, 2006.

[56] B. S. Instruments, *EC-LAB Software: Techniques and Applications*, 2011.

[57] A. Kneer, N. Wagner, C. Sadeler, A.-C. Scherzer, and D. Gerteisen, "Effect of dwell time and scan rate during voltage cycling on catalyst degradation in PEM fuel cells", *Journal of The Electrochemical Society*, vol. 165, no. 10, F805, 2018.

[58] C. Qin, J. Wang, D. Yang, B. Li, and C. Zhang, "Proton exchange membrane fuel cell reversal: a review", *Catalysts*, vol. 6, no. 12, p. 197, 2016.

[59] J.-H. Jang, H.-C. Chiu, W.-M. Yan, and W.-L. Sun, "Effects of operating conditions on the performances of individual cell and stack of PEM fuel cell", *Journal of Power Sources*, vol. 180, no. 1, pp. 476–483, 2008.

[60] B. Wahdame, D. Candusso, and J.-M. Kauffmann, "Study of gas pressure and flow rate influences on a 500 W PEM fuel cell, thanks to the experimental design methodology", *Journal of power sources*, vol. 156, no. 1, pp. 92–99, 2006.

[61] F. Barbir, *PEM fuel cells: theory and practice*. Academic press, 2012.

[62] A. Forrai, H. Funato, Y. Yanagita, and Y. Kato, "Fuel-cell parameter estimation and diagnostics", *IEEE transactions on energy conversion*, vol. 20, no. 3, pp. 668–675, 2005.

[63] S. Caux, J. Lachaize, M. Fadel, P. Shott, and L. Nicod, "Modelling and control of a fuel cell system and storage elements in transport applications", *Journal of Process Control*, vol. 15, no. 4, pp. 481–491, 2005.

[64] M. Becherif, A. Saadi, D. Hissel, A. Aboubou, and M. Y. Ayad, "Static and dynamic proton exchange membrane fuel cell models", *Journal of Hydrocarbons Mines and Environmental Research*, vol. 2, no. 1, 2011.

[65] A. Emerson and L. Montville, "Electrochemical characterization and water balance of a PEM fuel cell", *Worcester Polytechnic Institute: Worcester, MA, USA*, 2010.

[66] S. Touré, A. Konaté, D. Traoré, and D. Fofana, “Novel determination method of charge transfer coefficient of PEM fuel cell using the Lagrange’s multiplier method”, in *IOP Conference Series: Earth and Environmental Science*, IOP Publishing, vol. 188, 2018, p. 012 041.

[67] P. Khadke, T. Tichter, T. Boettcher, F. Muench, W. Ensinger, and C. Roth, “A simple and effective method for the accurate extraction of kinetic parameters using differential Tafel plots”, *Scientific reports*, vol. 11, no. 1, p. 8974, 2021.

[68] J. Kim, S.-M. Lee, S. Srinivasan, and C. E. Chamberlin, “Modeling of proton exchange membrane fuel cell performance with an empirical equation”, *Journal of the electrochemical society*, vol. 142, no. 8, p. 2670, 1995.

[69] A. Raman, P. Penas, D. van der Meer, D. Lohse, H. Gardeniers, and D. F. Rivas, “Potential response of single successive constant-current-driven electrolytic hydrogen bubbles spatially separated from the electrode”, *Electrochimica Acta*, vol. 425, p. 140 691, 2022.

[70] A. Holewinski and S. Linic, “Elementary mechanisms in electrocatalysis: revisiting the ORR Tafel slope”, *Journal of The Electrochemical Society*, vol. 159, no. 11, H864, 2012.

[71] B. Tartakovsky, M.-F. Manuel, H. Wang, and S. Guiot, “High rate membraneless microbial electrolysis cell for continuous hydrogen production”, *International Journal of Hydrogen Energy*, vol. 34, no. 2, pp. 672–677, 2009.

Appendix A

Design of PEMFC plates

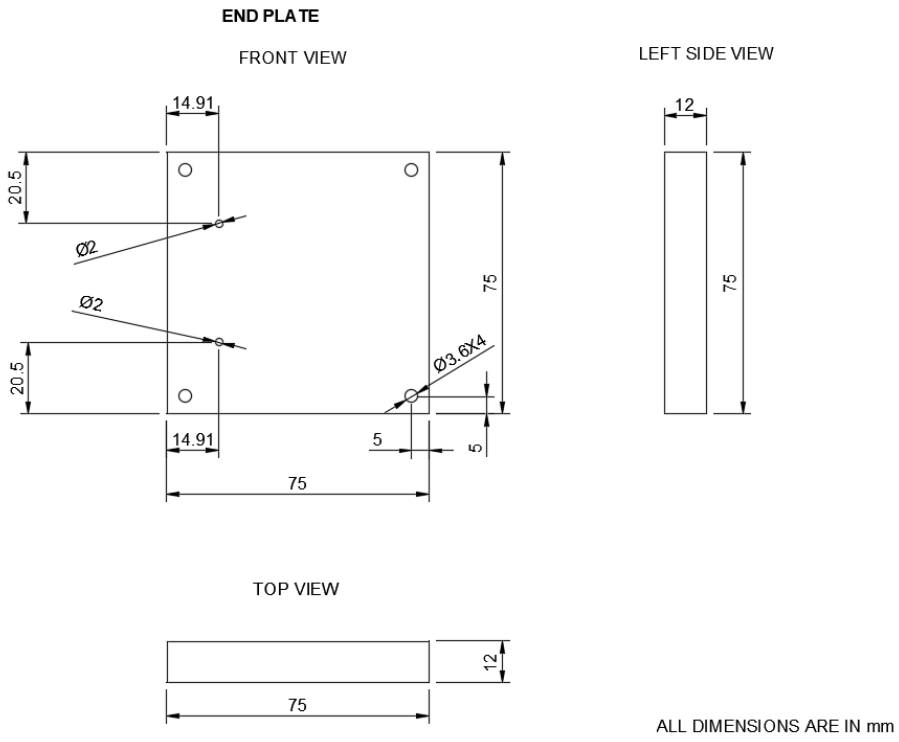

Figure A.1: Design of end plate.

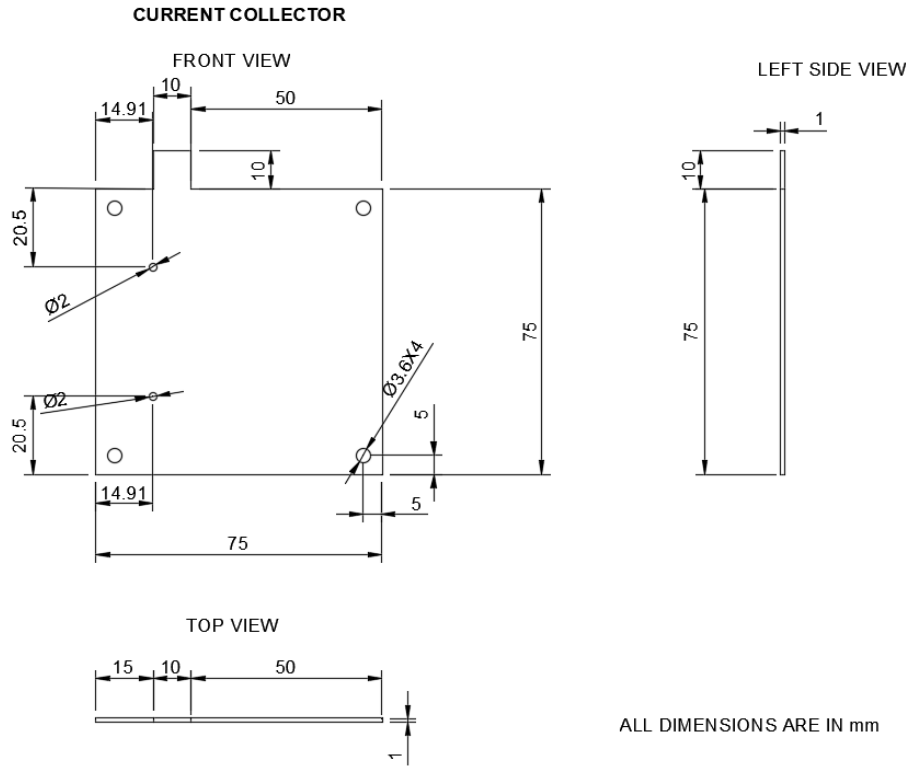

Figure A.2: Design of current collector.

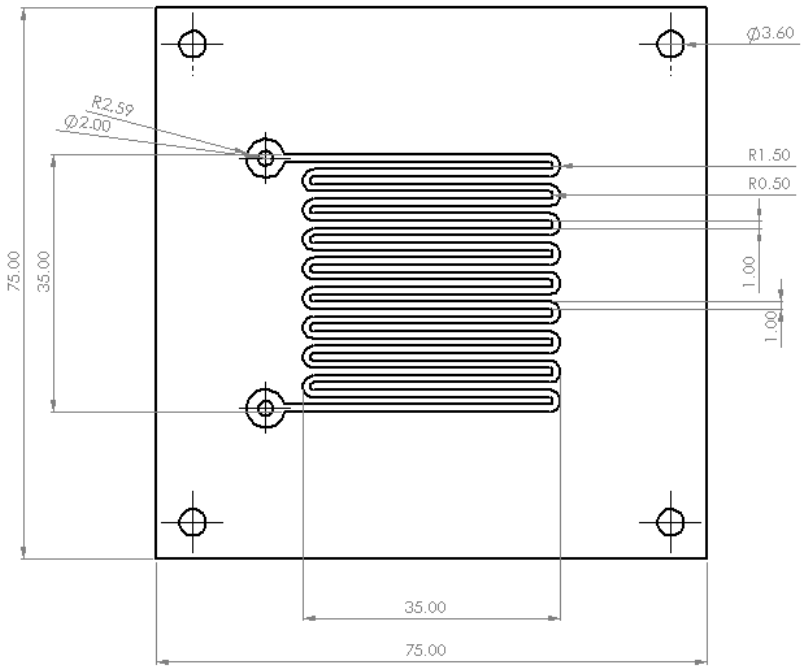

Figure A.3: Design of flow field plate (FFP) (active area: 3.5×3.5 cm^2).

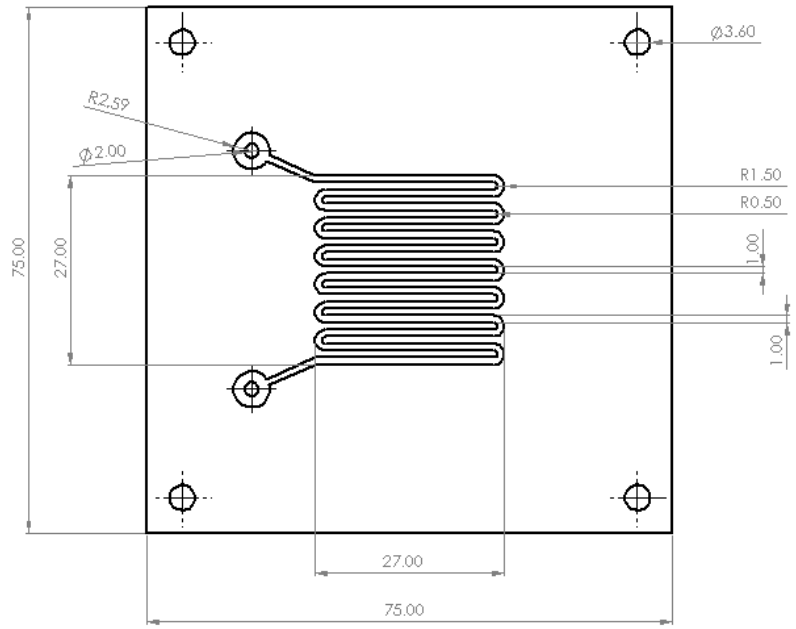

Figure A.4: Design of FFP (active area: 2.7×2.7 cm^2).

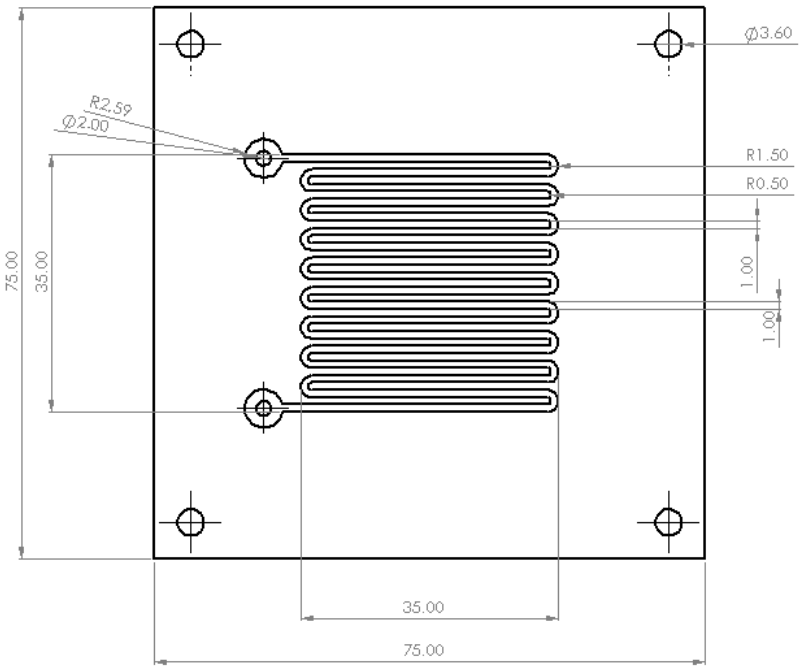

Figure A.5: Design of (FFP active area: 1.6×1.6 cm^2).

Appendix B

Experimental setup - Supplementary information

B.1 Design of sealing layers

Teflon gaskets were provided between the MEA and the graphite FFPs. Viton gaskets were provided between the current collectors and the end plates. A Teflon frame was used to hold the MEA in place. The gaskets and frames are collectively denoted as sealing layers (SLs). The design of the sealing layers is shown in Table B.1 (next page).

Table B.1: Design specifications for sealing layers

SL	**Part A**	**Part B**	**Distance between parts A and B** t_1 **[mm]**	**Material of SL**	**Thickness of one SL** t_2 **[mm]**	**Number of SLs on each side** n **[no units]**	**Combined thickness** t_3**=**Σ**n.**t_2 **[mm]**	**Compression** $\frac{t_1-t_3}{t_1}$**.100 [%]**	**Total number of SLs required for 3 PEMFCs [no units]**
Frame for MEA	Gasket	MEA	0.0545	Teflon	0.0508	1	0.0508	6.79	3
Gasket	FFP	MEA	0.39775	Teflon	0.254	1	0.3556	10.6	6
					0.0508	2			12
Gasket	End plate	Current collector	not fixed	Viton	0.7874	1	0.7874	0	2

B.2 Fluid adapters

A pair of 1/4-28” flat-bottom connectors were used to connect the inlet ports of PEMFCs at the end plates to Teflon tubes (inner diameter: 1.6 mm, outer diameter: 3.2 mm) with a pair of flangeless ferrules of material Ethylene tetrafluoroethylene (ETFE) (specifications: 1/4-28 Flat-Bottom, for 1/8” OD).

A pair of the following components were used in the fluid connections between the PEMFC and the electrolyzer.

Table B.2: Fluid connectors or adapters used in the experimental setup.

Connector	**Material**	**Through hole diameter [mm]**	**Specifications**
Luer lock adapter	Polyetheretherketone (PEEK)	1.3	thread port configuration: female to female, 1/4-28” flat-bottom
Barbed adapter	Polypropylene	1.25	Inner diameter: 1.6mm
Flangeless fitting	Delrin	1.6	1/4-28” flat-bottom
Ferrules	Ethylene tetrafluoroethylene (ETFE)	1.6	1/4-28” flat-bottom

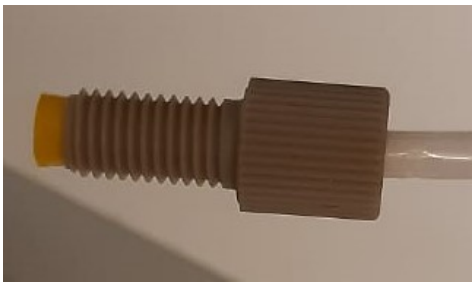

Figure B.1: Flangeless fitting and ferrule (1/4-28”, flat bottom connector).

Figure B.2: Barbed adapter (transparent), Luer lock adapter (red), and flangeless fitting (blue).

B.3 Potentiostat

There are 3 terminals in a potentiostat: working electrode, counter electrode, and the reference electrode. The reference electrode is fixed at some reference voltage (typically 0 V). The working electrode measures the variable potential of an electrode relative to the reference electrode. The counter electrode allows the current to flow through the external load circuit.

B.4 Supplementary visuals of the experimental setup

Figure B.3: Metal fasteners wrapped with teflon tape.

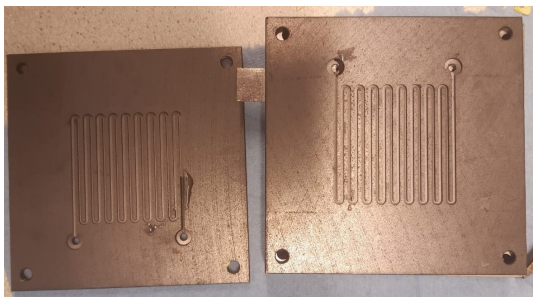

Figure B.4: Water in FFPs as a result of fuel cell reaction, after loading experiments (active area: 3.5×3.5 cm^2).

Appendix C

Linear fitting on Tafel plots

The derivation of activation parameters: transfer coefficient (α) and exchange current (I_0) is as follows.

Irreversible overpotentials (voltage losses) reduce the cell potential when the cell is loaded,

$$E_{\text{cell}} = E_0 - \eta_{\text{act}} - \eta_{\text{Ohm}} - \eta_{\text{con}}. \tag{C.1}$$

The activation overpotential is dominant in the low-current region,

$$E_{\text{cell}} \approx E_0 - \eta_{\text{act}}. \tag{C.2}$$

Tafel kinetics neglect the anodic activation overpotential (Section 2.1.2),

$$E_{\text{cell}} \approx E_0 - \frac{RT}{\alpha F} \log\left(\frac{I}{I_0}\right), \tag{C.3}$$

$$\Rightarrow E_{\text{cell}} = E_0 - \frac{RT}{\alpha F} \log(I) + \frac{RT}{\alpha F} \log(I_0). \tag{C.4}$$

Equation C.4 is in the form of a straight line $y = -mx + c$ for the Tafel plot [61],

$$y = E_{\text{cell}}, \tag{C.5}$$

$$x = \log(I), \tag{C.6}$$

$$\text{slope, } m = \frac{RT}{\alpha F}, \tag{C.7}$$

$$\text{y-intercept, } c = E_0 + \frac{RT}{\alpha F} \log(I_0). \tag{C.8}$$

By fitting a straight line in the low-load current region of the Tafel plot [69], [70], the transfer coefficient α and exchange current I_0 can be found using equations C.7 and C.8. Such a linear fitting in the Tafel plots obtained from CV experiments done on a PEMFC (active area: 3.5×3.5 cm^2) are shown in Fig. C.1.

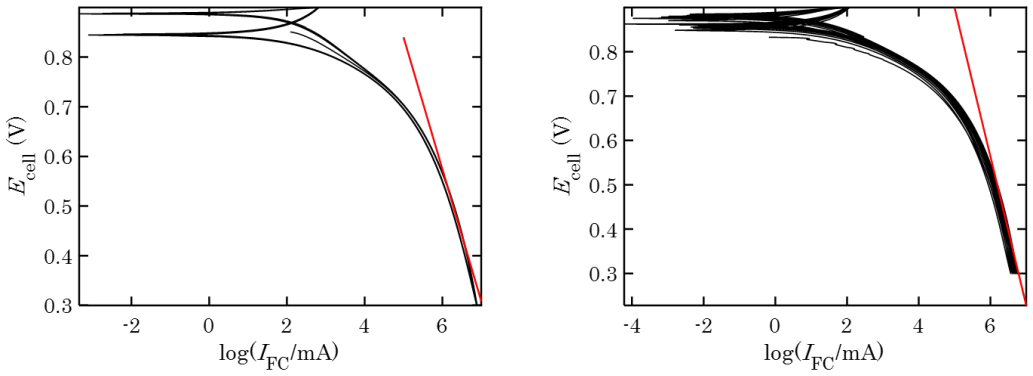

Figure C.1: Linear fitting on the Tafel plots for PEMFC (active area: 3.5×3.5 cm^2) for CV scan rates of (a) 100 mV.s^{-1} (b) 20 mV.s^{-1}.

The transfer coefficient and exchange current were found using equations (C.9) and (C.10) respectively,

$$\alpha = \frac{RT}{mF}, \tag{C.9}$$

$$I_0 = \exp\left(\frac{\alpha F}{RT}(c - E_0)\right). \tag{C.10}$$

Table C.1: Exchange current I_0 and transfer coefficient α for PEMFCs of different active areas from linear fitting in Tafel plots from CV experiments with different scan rates.

MEA active area [cm×cm]	$\frac{dE}{dt}$**=100 mV.s^{-1}**		$\frac{dE}{dt}$**=20 mV.s^{-1}**	
	α **[no units]**	I_0 **[mA]**	α **[no units]**	I_0 **[mA]**
3.5 × 3.5	0.0956	127.8293	0.0757	157.4686
2.7 × 2.7	0.0823	41.0274	0.0615	59.1088
1.6 × 1.6	0.0719	34.8778	0.0605	39.5995

The linear fitting in Tafel plots for other PEMFCs are given below.

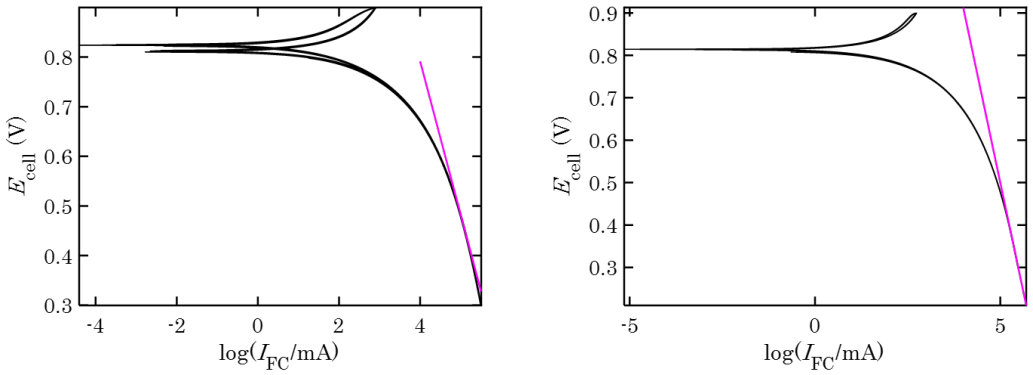

Figure C.2: Linear fitting on the Tafel plots for PEMFC (active area: 2.7×2.7 cm^2) for CV scan rates of (a) 100 mV.s^{-1} (b) 20 mV.s^{-1}.

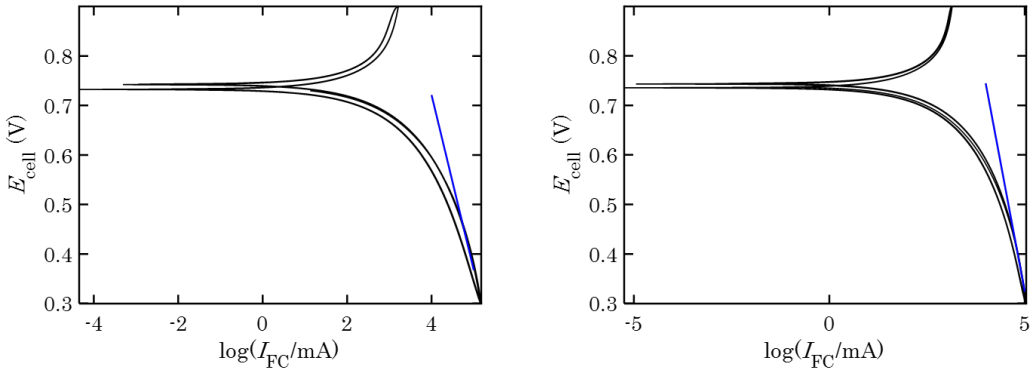

Figure C.3: Linear fitting on the Tafel plots for PEMFC (active area 1.6×1.6 cm^2) for CV scan rates of (a) 100 mV.s^{-1} (b) 20 mV.s^{-1}.

Appendix D

Ohmic drop measurements

Ten trials of ZIR experiments were performed to measure the Ohmic resistance of the PEMFCs by measuring the high-frequency impedance of the cells. The mean resistance and standard deviation resistance for each PEMFC is given in Table D.1.

Table D.1: Ohmic resistance of PEMFCs of different active areas

MEA active area (cm $\times$ cm)	**Mean resistance, R_{FC} (Ω)**	**Standard deviation (Ω)**
3.5 $\times$ 3.5	0.3748	0.0547
2.7 $\times$ 2.7	0.746	0.0279
1.6 $\times$ 1.6	2.9686	0.2249

Appendix E

At no-load cell potential (OCV) state

E.1 Effect of electrolyzer current (flow rates of reactants) on OCV

The molar flow rates of reactants to the PEMFC(s) depend linearly on the electrolyzer current from Faraday's law of electrolysis (equation E.1)

$$\dot{n} = \frac{I_{\mathrm{EL}}}{zF}, \tag{E.1}$$

where z is the number of electrons per mole. It is 2 for hydrogen and 4 for oxygen based on the fuel cell redox reaction.

1 mol of hydrogen is equivalent to 22.4 L in volume at STP [71]. The ideal gas law is given as

$$PV = nRT, \tag{E.2}$$

where P and T are the pressure and temperature of the gas respectively. n and V are the number of moles and volume of the gas respectively. R is the gas constant.

Assuming other parameters to be constant, at a cell operating temperature of T, 1 mol of hydrogen is equivalent to $\frac{T}{273.15} \cdot 22.4$ [L]. Therefore the molar flow rate depends linearly on the volumetric flow rate,

$$\dot{V} = \frac{T}{273.15} \cdot 22.4 \cdot \dot{n} \quad [\mathrm{L.s^{-1}}]. \tag{E.3}$$

Therefore there is a linear relation between the electrolyzer current and the volumetric flow rate of gases supplied by the electrolyzer to the PEMFC.

Fig. E.1 indicates that the volumetric flow rate of reactants, controlled by the electrolyzer current, does not influence the no-load cell potential (OCV) of the PEMFCs. The plot also suggests that the partial pressure of reactants is almost constant for different reactant flow rates from Nernst equation (E.4).

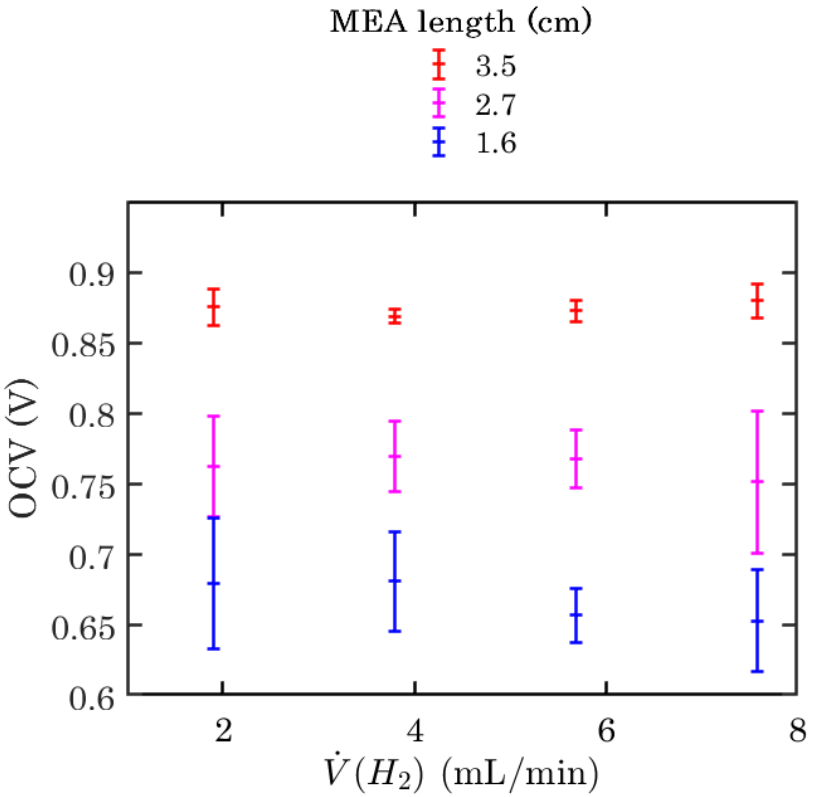

Figure E.1: OCV variations with flow rates of hydrogen for PEMFCs of different active areas

E.2 Partial pressure of Hydrogen at OCV

The Nernst equation (E.4) provides a relation between the Open Circuit Voltage (OCV) (E_0), and the partial pressures of the reactant gases,

$$E_0 = E_r + \frac{RT}{zF} \log \left(\frac{p_{\mathrm{H_2}}^2 \cdot p_{\mathrm{O_2}}}{p_{\mathrm{H_2O}}^2} \right). \tag{E.4}$$

The partial pressure of water, $p_{\mathrm{H_2O}}$ was considered as 1 atm (1.01325 bar) since water was discharged in liquid phase. The partial pressure of oxygen, $p_{\mathrm{O_2}}$ was considered as $0.21 \cdot P_{\mathrm{atm}}$ (Section 5.3).

The average OCVs for PEMFCs in descending order of their active areas are 0.87 V, 0.75 V, and 0.65 V respectively.

The corresponding partial pressures of hydrogen were found using equation E.4. Fig. E.2 shows the relation between the average recorded OCV and the partial pressure of hydrogen.

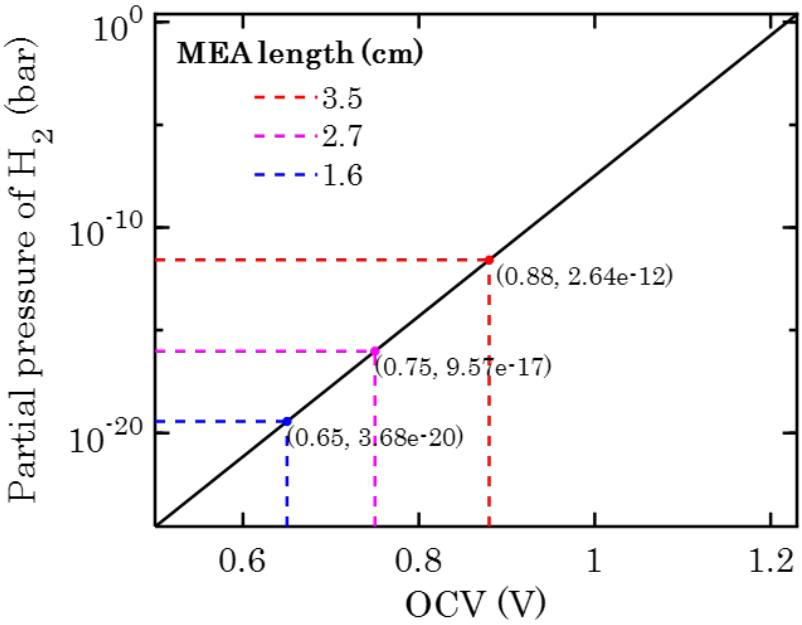

Figure E.2: Plot of Open Circuit Voltage (OCV) versus the partial pressure of hydrogen for PEMFCs of different active areas.

This plot also verfies that the partial pressure of hydrogen, p_{H_2} is almost neglegible.

Appendix F

Fuel cell efficiency

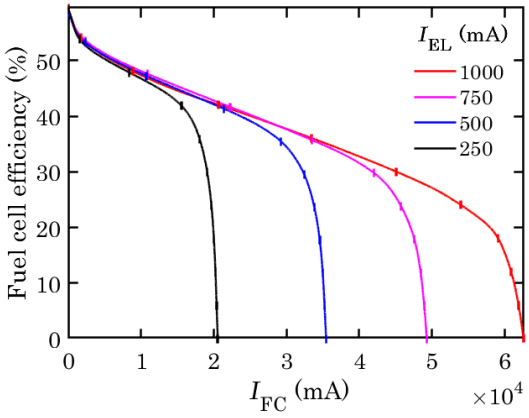

Figure F.1: Fuel cell efficiencies for PEMFC (active area: 3.5×3.5 cm^2) for different electrolyzer currents, I_{EL} = 1000, 750, 500, and 250 [mA].

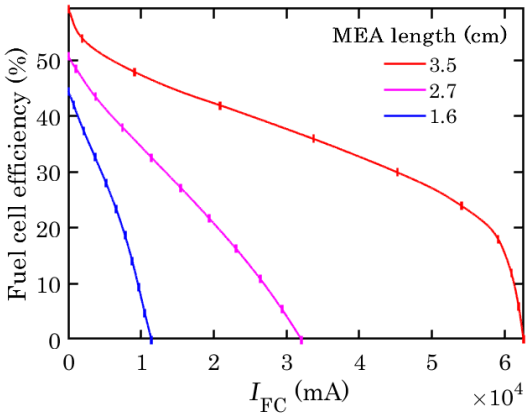

Figure F.2: Fuel cell efficiencies for different load currents for PEMFCs of different active areas: 3.5×3.5 cm^2, 2.7×2.7 cm^2, and 1.6×1.6 cm^2 for $I_{\mathrm{EL}} = 1$ A.